

QUANTITATIVE PROBES OF BACTERIAL PHYSIOLOGY

A Dissertation

by

KATHY YEONJOO RHEE

Submitted to the Graduate and Professional School of
Texas A&M University
in partial fulfillment of the requirements for the degree of

DOCTOR OF PHILOSOPHY

Chair of Committee, Pushkar P. Lele
Committee Members, Jennifer Herman
Paul Straight
Victor Ugaz
Head of Department, Arul Jayaraman

May 2022

Major Subject: Chemical Engineering

Copyright 2022 Kathy Yeonjoo Rhee

ABSTRACT

All major processes in living systems depend on energy sources. In bacteria undergoing cellular respiration, the central source of energy is the proton motive force (PMF). In addition to ATP synthesis, the PMF directly powers numerous other functions including motility, chemotaxis and cell division. Despite its importance, methods to quantify the PMF in live bacteria are limited. For this reason, the dependence of motility on the PMF is particularly interesting as the former could be used as a quantitative readout of the latter. In this work, we have developed protocols to quantitatively probe the PMF in different bacterial species. We systematically tested the relation between motility and the PMF in a multi-flagellated species – *Bacillus subtilis*. Specifically, we measured the relationship between the membrane potential, which is a component of the PMF, and the swimming speeds of individual bacteria. We then compared the swimming speeds against flagellar rotation rates. Comparisons with *Escherichia coli* revealed that hydrodynamic factors complicate the PMF/flagellar rotation/swimming speed relationships in peritrichous (multi-flagellated) species. Next, we quantified the second component of the PMF – the transmembrane pH gradient - by characterizing pH-sensitive fluorescence proteins in *E. coli*. We developed a scaling analysis that overcame some of the limitations of the green fluorescent protein (GFP); specifically, the dependence of emissions on protein concentrations. Finally, we worked with a monotrichous bacterial species, *Caulobacter crescentus*, as their motility is relatively straightforward to interpret owing to the presence of a single flagellum. As the strategies of chemotaxis are poorly understood

in this species, we focused on the response of *C. crescentus* to multiple chemoeffectors. We observed that *C. crescentus* is poor in chemotaxis despite possessing a rather complicated and elaborate chemotaxis network. It is likely that the so-called chemotaxis network in *C. crescentus* has a primary function that is different from chemotaxis.

DEDICATION

Dedicated to my parents who encouraged and supported me to pursue a doctoral degree. Thank you for always believing in my potential.

ACKNOWLEDGEMENTS

I would like to thank my committee chair, Dr. Lele, and my committee members, Dr. Herman, Dr. Straight, and Dr. Ugaz, for their guidance and support throughout the course of this research.

Thanks also go to my friends and colleagues and the department faculty and staff for making my time at Texas A&M University a great experience. A special thanks to the past and current members of the Lele lab for all the discussions, times inside the lab, and being a great company. A special thanks to Amy for helping me adjust to life in College Station. Thanks also goes to Matt who had to listen to all my ups and downs throughout graduate school. Thanks for your patience.

Finally, thanks to my parents and my brother for their continual encouragement. I could not have made it without their support and love.

CONTRIBUTORS AND FUNDING SOURCES

Contributors

This work was supervised by a dissertation committee consisting of Dr. Pushkar Lele (advisor) and Dr. Victor Ugaz of the Department of Chemical Engineering and Dr. Jennifer Herman of the Department of Biochemistry and Biophysics and Dr. Paul Straight of the Department of Biochemistry and Biophysics and the Department of Genetics.

Chapter 3 contains the work from “Protein expression-independent response of intensity-based pH-sensitive fluorophores in *Escherichia coli*” published in Plos One in 2020. The conceptualization and the development of the methodology in Chapter 3 was conducted in part by Ravi Chawla. Chapter 4 and Chapter 5 includes manuscript currently under preparation. The analyses depicted in Chapter 5 were conducted in part by Aaryan Sharma.

All other work conducted for the dissertation was completed by me independently under the supervision of Dr. Pushkar Lele.

Funding sources

Graduate study was supported by a fellowship from the Texas A&M University. This work was also supported in part by grants from National Institutes of General Medical Sciences Health (R01-GM123085) and the Department of Defense ACC-APG-RTP Division (W911NF1810353) to Dr. Pushkar Lele. The funders had no role in study design, data collection and analysis, decision to publish, or preparation of the manuscript.

NOMENCLATURE

CCW	Counter-clockwise
CW	Clock-wise
Fps	Frames per second
GEVI	Genetically-encoded voltage indicators
GFP	Green fluorescent protein
LB	Luria broth
MB	Motility buffer
OD ₆₀₀	Optical density at 600 nm
PMF	Proton motive force
PYE	Peptone yeast extract
SMF	Sodium motive force
TB	Tryptone broth

TABLE OF CONTENTS

	Page
ABSTRACT	II
DEDICATION	IV
ACKNOWLEDGEMENTS	V
CONTRIBUTORS AND FUNDING SOURCES.....	VI
NOMENCLATURE.....	VII
TABLE OF CONTENTS	VIII
LIST OF FIGURES.....	XI
LIST OF TABLES	XIII
CHAPTER I INTRODUCTION.....	1
CHAPTER II BACKGROUND.....	4
Proton motive force.....	4
Bacterial motility.....	7
Chemotaxis.....	10
CHAPTER III PROTEIN EXPRESSION-INDEPENDENT RESPONSE OF INTENSITY-BASED PH-SENSITIVE FLUOROPHORES IN <i>ESCHERICHIA COLI</i> *	13
.....	13
Introduction.....	13
Materials and Methods.....	16
Cell culturing.....	16
Modulation of intracellular pH.....	16
Fluorescence assays.....	17
Statistical testing.....	18
Results.....	20
pH-sensitive fluorophore emission.....	20
Analytical model to eliminate dependence of signals on expression levels.	23

Dependence of ratiometric emission ratios on illumination and detection conditions	26
Dynamic range and sensitivity of intensity-based probes	28
Discussion	30
Supplementary Information.....	33
Supplementary figures.....	33
Supplementary equations 1	34
Supplementary equations 2	35

CHAPTER IV QUANTIFICATION OF PROTON MOTIVE FORCE VIA SWIMMING SPEED IN MULTI-FLAGELLATED BACTERIA 37

Introduction	37
Materials and Methods	39
Strains and media	39
Swimming speed and cell size.....	39
Hook and filament fluorescent labeling	40
Flagellar rotation rate	41
Membrane potential measurements.....	42
Results	42
Flagellar rotational speed	42
Swimming speed and cell length.....	43
Flagellar geometry.....	44
Flagellar number.....	45
Predicted rotational speed based on slender body theory.....	47
Direct comparison of swimming speed and membrane potential	48
Discussions.....	51
Supplementary Information.....	53

CHAPTER V CHEMOTAXIS IN *CAULOBACTER CRESCENTUS* 55

Introduction	55
Materials and Methods	57
Cell culturing.....	57
Motor rotational measurements.....	58
Capillary assay	58
Transwell assay	59
Results	60
Single cell flagellar dynamics	60
Capillary assay	62
Transwell assay to test longer dynamics	66
Discussions.....	68
Supplementary Information.....	69

CHAPTER VI CONCLUSIONS AND FUTURE WORK.....	71
REFERENCES.....	74

LIST OF FIGURES

	Page
Figure III-1. Schematic of the experimental set-up.....	19
Figure III-2. pH-sensitive emission intensities for fluorophores.	22
Figure III-3. Normalized emission intensities and ratios as a function of cytoplasmic pH.	26
Figure III-4. Dynamic range in pH measurements.....	29
Figure III-5. Fluorophore sensitivity versus pH.....	30
Figure III-6. Relative expression levels of Gfpmut3* at different IPTG concentrations.	33
Figure III-7. Emissions from pH-insensitive DsRed-Express.....	34
Figure IV-1. Motor rotational speed measurements for <i>E. coli</i> and <i>B. subtilis</i>	43
Figure IV-2. Swimming speed and cell length measurements.....	44
Figure IV-3. Fluorescently labeled filaments and their numbers.....	46
Figure IV-4. Fluorescently labeled hooks.	47
Figure IV-5. Swimming <i>B. subtilis</i> in the presence of CCCP.....	49
Figure IV-6. Fluorescence intensity of ThT over time.....	50
Figure IV-7. Change in swimming speed versus change in membrane potential.	51
Figure IV-8. Bundle diameter measurement of swimming bacteria.	54
Figure IV-9. Polymorphic form of flagella.	54
Figure V-1. Schematic of transiently tethered cells.	61
Figure V-2. Flagellar motor dynamic changes with xylose concentration.....	62
Figure V-3. Schematic of the modified capillary assay	63
Figure V-4. Number of cells with exposure to a point source.	65

Figure V-5. Relative number of cells with exposure to a point source.	66
Figure V-6. The observed chemotaxis response using transwell assay.	67
Figure V-7. Basal level in the number of cells over time for <i>C. crescentus</i> strains.	69
Figure V-8. Swimming speed of <i>C. crescentus</i>	70

LIST OF TABLES

	Page
Table III-1. Filter information.....	20
Table IV-1. Flagellar geometry.....	45
Table IV-2. Strain list.....	53

CHAPTER I INTRODUCTION

The proton motive force (PMF) plays a major role in impacting cellular physiology. The PMF aids in bacterial proliferation as it powers various cellular processes such as ATP synthesis, cell division, pH homeostasis, and bacterial motility. Changes in the PMF can also promote pathogenicity and antibiotic resistance. Therefore, accurate quantification of the PMF is needed for fundamental insights into important cellular processes. In this work, we focused on developing facile techniques to measure the PMF and its effects on two major fitness factors: motility and chemotaxis.

PMF consist of two components: the membrane potential and the pH gradient across the membrane. In Chapter 2, we review the available methods for quantifying each component and discuss their limitations. We discuss the link between the PMF and bacterial motility. We distinguish between peritrichous and monotrichous bacteria to emphasize how swimming speeds of individual cells could help estimate the PMF provided we account for the positioning of the flagella on the cell body.

In Chapter 3, we have determined how pH-sensitive fluorescent proteins could be used as quantitative probes of the intracellular pH. A key limitation of fluorescent proteins such as GFP (Green fluorescent protein) is the dependence of photon emission on protein concentrations. To eliminate this limitation, we developed a mathematical model for normalizing the emission vs pH relationships. We tested the model with several fluorescent proteins that modulate their emission intensities as a function of the pH. These proteins exhibit two states with distinct spectra: protonated and deprotonated. Changes in

the pH induce an equilibrium shift between the two states. Comparisons between experiments and the model suggested that our scaling analysis was successful in eliminating the dependence of the pH response on protein expression levels, which makes these probes better in some regard to ratiometric fluorescent probes. We anticipate our framework will help extend the applications of intensity-based pH reporters for pH-sensitive measurements.

In Chapter 4, we tested bacterial motility as a probe of the PMF. Previous measurements in *Escherichia coli* suggested that the flagellar rotation rates are linearly dependent on the PMF. This relationship has not been measured in other bacterial species. As swimming speeds are easier to quantify compared to flagellar rotational speeds, we characterized the membrane potential vs swimming speed relationships in two model organisms, Gram-negative *E. coli* and Gram-positive *Bacillus subtilis*. We recorded what appeared to be a linear regime in the potential vs swimming speed curves for *B. subtilis*. This experimental plot is expected to help estimate changes in the PMF directly from swimming speed in *B. subtilis*. We also compared the swimming speeds in *E. coli* and *B. subtilis*: their swimming speeds were similar despite the flagellar rotation rates being slower in the latter species. To account for differences in hydrodynamic thrust in the two species, we measured various properties such as flagellar rotation rate, swimming speed, cell geometry, flagellar geometry, and flagellar number. Our work suggested that a simple hydrodynamic analysis is inadequate to predict flagellar rotation rates from swimming speeds in peritrichous bacteria – put differently, theoretical (but not experimental)

estimation of PMF changes from observed changes in swimming speeds is unlikely to be accurate without accounting for hydrodynamic interactions within flagellar bundles.

Caulobacter crescentus carries a single polar flagellum, and it does not suffer from some of the hydrodynamic complications that are observed in peritrichous bacterial species. It is, therefore, an excellent model system to study the effects of PMF on swimming speeds. However, very little is known about motility and chemotaxis in this species. Therefore, we shifted our attention to characterizing chemotaxis in this species in Chapter 5. We investigated the chemotactic response of *C. crescentus* to various chemical stimulants. Our analysis revealed only a weak or negligible chemotactic response towards major stimulants. Although the presence of chemical stimulants induced a change in the reversal frequency between forward and backward swimming modes, a strong correlation was absent with chemotactic performance. These measurements suggest that *C. crescentus* is unlikely to exhibit strong chemotaxis. It is likely that chemotaxis effects are unlikely to confound the interpretation of PMF vs motility relationships, which will be the subject of future work.

CHAPTER II BACKGROUND

Proton motive force

Chemiosmotic theory by Peter Mitchell states that the electrochemical potential of ions across the membrane drives adenosine triphosphate (ATP) synthesis. [1, 2]. This electrochemical gradient, called the proton motive force (PMF), is generated from the pumping of the protons during electron transport. PMF consists of two components: membrane potential and pH gradient across the membrane as shown by the equation:

$$PMF = \Delta\psi + 2.3 \left(\frac{k_B T}{e} \right) \Delta pH$$

where $\Delta\psi$ is the transmembrane electric potential, k_B is the Boltzmann constant, T is the absolute temperature, and e is the proton charge, and ΔpH is the pH difference across the membrane. At room temperature, $2.3*(k_B T/e)$ is approximately 60 mV. Recent studies revealed that PMF regulates not only the ATP synthesis but a wide range of bacterial physiology and functions, such as antibiotic resistance [3], persister formation [4], pH homeostasis [5], cell division [6], dynamic communication [7, 8], membrane transport [9], and cell motility [10, 11]. As these processes are essential for cell proliferation, accurate quantification of PMF is desired.

However, measuring PMF in bacteria is not a straightforward, especially because of its small size. In eukaryotic cells, one can directly measure the PMF using patch clamp method by impaling cells with microelectrodes. However, bacterial cells are usually too small to be impaled. It has only been successful under non-physiological conditions, where

the cells are treated to become large like spheroplasts and protoplasts [12-14]. Therefore, PMF in bacteria needs to be measured indirectly.

Bacterial membrane potential is measured using fluorescent probes like Nernstian dyes, membrane-bound dyes, and genetically-encoded voltage indicators (GEVIs). Among these, Nernstian dyes such as are most popular – especially fluorescent cationic lipophilic dyes like Rhodamine 123, (DiOC₂)³, and Thioflavin T [7, 8, 15-21]. Membrane potential can be determined experimentally by measuring the fluorescence intensity as it is proportional to the ion concentration. However, there are some disadvantages. Due to its positive charge, high concentration of the dye can lower the membrane potential [22]. Additionally, dynamic measurements become complicated due to dye transport properties. Finally, variable permeability of the dye between Gram-positive and Gram-negative bacteria complicates interspecies comparison [21]. To overcome accumulation of Nernstian dyes inside the membrane, membrane-bound dyes such as aminonaphthylethenylpyridinium (ANEP) dyes can be used. A variant of ANEP dyes, di-4-ANEPPS, has been used to measure membrane potential in *Saccharomyces cerevisiae* [23] and *Candida albicans* [24]. Depending on the membrane potential, the dye shifts its excitation spectra. Compared to Nernstian dyes, the captured response is faster, but has a lower signal-to-noise ratio. Lastly, a GEVI, specifically proteorhodopsin optical proton sensor (PROPS), provided membrane potential measurements in bacteria [25-27]. But one of the potential drawbacks is its effects on physiology may be unpredictable. Although these measurements provide valuable information on the membrane potential, they do not provide any information on the second component of PMF – pH. Because these two

components counteract and compensate for changes in the other, both must be measured for an accurate value of PMF [28, 29].

Several methods have been employed to measure the cytoplasmic pH. Most pH probes operate by changing their properties based on the external pH, which included radioactivity and chemical shifts [30, 31]. However, these probes suffered from complicated set-ups making pH measurements difficult. This led to the rise of using pH-sensitive fluorescent proteins, since these proteins are expressed intracellularly. Recently, pH-sensitive ratiometric fluorescent proteins, pHluorin, have gained popularity for its independence on protein expression levels [32]. However, it suffers from the necessity of an expensive multi-wavelength excitation setups which also make dynamic measurements difficult. Possible cell toxicity due to the blue light effect is also a problem. Instead of ratiometric probes, a simple single-excitation, single-emission green fluorescent protein (GFP) is preferred. Unfortunately, fluorescence signal is proportional to the number of fluorescent proteins, thus making the fluorescence signal dependent on protein concentrations, which can vary significantly from cell to cell. This limits the application of pH-sensitive GFP. In Chapter 3, we establish methods to overcome the signal dependence on protein concentration of GFP.

The described methods have been used to study the magnitude of $\Delta\psi$ and ΔpH contribution to PMF. At times, the membrane potential has been regarded as analogous to the PMF, but this is largely untrue. The ΔpH contribution to the PMF can often fluctuate because bacteria maintain their internal pH over wide ranges of external pH. The ΔpH contribution to PMF for neutralophile *E. coli* (intracellular pH ~ 7.8) is approximately -

48mV when the external pH is 7.0. The contribution of $\Delta\psi$ is approximately -120 mV, making up a total PMF of -168 mV. However, the ratio of ΔpH and $\Delta\psi$ to PMF changes over external pH as they compensate for one another. At external pH of 5.5, the ΔpH increases to -138 mV. The large ΔpH is partially offset by the membrane potential: $\Delta\psi$ was measured to be ~100 mV [28]. Therefore, with certain environments, the ΔpH component is larger than $\Delta\psi$. This is especially true for acidophiles such as *Acidithiobacillus ferrooxidans* which survive at pH 2. To offset the extremely large ΔpH , the $\Delta\psi$ is reversed, where the inside the membrane is more positive relative to the outside. In this case, the ΔpH is -266 mV while $\Delta\psi$ is +10 mV [5, 33]. Therefore, it is crucial to measure both components of the PMF.

Given the technical challenges in quantifying the two PMF components simultaneously, other methods are sought. The dependence of bacterial motility on the PMF is of particular interest as the former can be used as quantitative readout of the latter [11], overcoming some of the challenges with PMF measurements in live bacteria. In Chapter 4, we elaborate on our efforts to measure the PMF from motility in peritrichous bacterial species – bacteria carrying more than one flagellum on their bodies.

Bacterial motility

One of the key physiological processes that is powered by the PMF is bacterial motility [10]. Bacteria swim by rotating helical filaments known as flagella [34]. Each flagellum is attached to a rotary motor via a flexible hook. The rotary motor operates by coupling the ion flux across the membrane to motor rotation [35-37]. In turn, the motor

rotates the flagellar filament. The direction of rotation can switch between counterclockwise (CCW) or clockwise (CW) direction, enabling the bacteria to navigate their surroundings. Bacterial motility has been extensively studied in the Gram-negative model organism, *E. coli*. Because PMF powers the motor rotation, motor rotation speeds can be used to estimate PMF changes [38].

Measuring the motor rotational speed can be challenging as the flagellum is difficult to visualize under simple phase microscopy. To overcome this, a tethered cell assay is typically employed. The first tethered cell assays involved a polyhook mutant of *E. coli* and anti-hook antibodies to tether hooks to a glass substrate, causing the cell body to rotate [39]. An improvement was made when a sticky flagellar mutant was created in *E. coli* [40, 41]. This mutant allowed studying the flagellar motor response to environmental stimuli and viscous loads [42-44]. The sticky flagellar mutant is sheared to short stubs and is attached either to the glass substrate (tethered cell assay) or polystyrene beads (bead assay). The cell body or the bead can be monitored to determine the flagellar rotation rate. Using these techniques, a linear relationship between the speed of the motor and PMF has been determined in a few bacterial species: -50 mV to -150 mV in *E. coli* [11, 45] and -30 mV to -100 mV in *Streptococcus* strain V4051 [46-48]. Therefore, flagellar rotation rate can serve as a good PMF probe. However, this assay is only well established in few species, and it has limited utility [49].

Recently, a sticky flagellar mutant in the Gram-positive model organism *B. subtilis* was developed by combining the sticky *fliC* allele from *Salmonella typhimurium* and the *hag* gene in *B. subtilis* [50]. The mutant in *B. subtilis* was especially useful to evaluate the

dynamics of stators in the flagellar motor of *B. subtilis* [50, 51]. Unlike *E. coli*, the *B. subtilis* motor has two distinct stator complexes: H⁺-type MotAB and Na⁺-type MotPS [52, 53]. MotAB is powered by the PMF, and the MotPS is powered by the sodium motive force (SMF). The assembly of MotPS is highly Na⁺-dependent and load-dependent. With increasing Na⁺ levels and viscous loads, the number of bound MotPS increases [50]. Therefore, the flagellar rotation rate is not only dependent on the PMF but also SMF. Especially load-inducing assays like tethered cell or bead assay increases the influence of SMF. MotPS, however, does not seem to be well-engaged with the motor during swimming, as the swimming speed does not change with the disruption of the MotPS complex [54, 55]. Therefore, the Na⁺ dependent MotPS stators are unlikely to complicate the analysis of swimming motility in *B. subtilis*.

One of the ways to measure the flagellar rotation rate is through fluorescent labeling of flagella. Flagellin proteins with a cysteine mutation in one of the surface-exposed sites is treated with a maleimide-based fluorescent dye. Laser illumination lights up the flagellar filament. Videos of labeled swimming cells are recorded at high frames per second (fps), to capture the full rotation of the flagella. By determining the number of frames for a full revolution, the flagellar rotation rate can be calculated [56]. However, these experiments are technically challenging as fast fps necessitates a small field of view, which decreases the probability of observing swimmers for adequate durations that are necessary for accurate analysis. Therefore, in Chapter 4, we explore using swimming speed instead to characterize PMF as swimming speed can be accurately determined with

simple phase microscopy, and the method is generally extensible to all motile bacteria without genetic modifications.

Chemotaxis

Chemotaxis is the migration of bacteria towards or away from a chemical stimulus. The first assay to confirm this was Adler's capillary assay [57]. This assay revealed that bacteria swam and accumulated towards the capillary in the presence of certain compounds – known as attractants. Chemotaxis is enabled by flagellar switching between CCW and CW directions. In peritrichous *E. coli*, CCW-rotating flagella form a bundle that thrusts the cell forward in a straight line – called a run [58]. Flagellar switching from CCW to CW causes the cell to tumble and switch direction. Run-tumble pattern promote chemotaxis in peritrichous species [56, 59, 60].

The run and tumbles are controlled by a signaling network – the chemotaxis network [61]. Chemical stimuli like attractants and repellents are sensed by methyl-accepting chemotaxis proteins (MCPs). In *E. coli*, there are five MCPs: four membrane-bound chemotaxis receptors (Tsr, Tar, Tap, and Trg) and one oxygen-sensing receptor (Aer). Upon sensing of a stimuli by the receptor, the activity of a chemotaxis kinase CheA is modulated. CheA, then, modulates the phosphorylation levels of a response regulator CheY. Phosphorylated CheY interacts with the flagellar rotor to promote a conformational change, which leads to a switch in the direction of rotation [31, 32]. In the presence of an attractant, the phosphorylation levels of CheY decreases, and the flagella rotates in CCW, and vice versa. Therefore, in peritrichous bacteria, the probability of CW rotation (CW_{bias}) is the key parameter in measuring chemotaxis.

However, the precise role of CW_{bias} modulation is debatable in polar-flagellated species. There are two types of polar-flagellates: monotrichous species carrying single flagellum like *C. crescentus*, *Pseudomonas aeruginosa*, and *Vibrio alginolyticus* and lophotrichous species carrying multiple flagella like *Helicobacter pylori*. Polar flagellates do not employ run-tumble pattern, but instead swim in a run-reversal manner. Depending on the handedness of the flagellum, the cell propels forward in one rotational direction and reverses in the other direction. *H. pylori* modulate their CW_{bias} , presumably for the purposes of chemotaxis [33]. However, in other species such as *C. crescentus* and *P. aeruginosa*, cells appear to modulate the reversal frequencies [62-64]. It is unclear whether polar-flagellates chemotax and if they do so by modulating either CW_{bias} or reversal frequency or both.

In Chapter 5, we investigated the chemotaxis mechanism of a polar-flagellate, *C. crescentus*, bacterium found in freshwater lakes and streams. *C. crescentus* possess a single, right-handed flagella located at the pole. Due to the filament's right-handedness, the cell swims forward when the flagellum rotates CW. It swims backward when the flagellum rotates CCW. The flagellated motile swarmer cell transitions into a sessile stalked cell by shedding its flagellum and synthesizing an adhesive holdfast. The major chemotaxis cluster is cell-cycle dependent, and the chemotaxis proteins are only expressed in motile cells [65-68]. Interestingly, a genomic scan of *C. crescentus* revealed that there are multiple copies of the chemotaxis proteins [69, 70]. Specifically, there are 18 independent genes coding for MCPs, which suggest that *C. crescentus* may sense a wide array of attractants and repellents. Additionally, there are 12 CheY proteins which can

modulate the motor response. One of the CheY protein in *C. crescentus*, CheYII, behaves similarly to the CheY in *E. coli*. Binding of the phosphorylated CheYII to the motor leads to a switch in the rotational direction to CCW and the cell swims backwards. However, as the function of other CheY proteins are less understood, it is unclear how these CheY homologs respond to chemoeffectors. It has been suggested that the other CheY homologs compete with CheYII by binding to the motor and modulating the swimming speed and motor switching rates [71, 72].

Why does *C. crescentus* need such a complicated network to simply modulate flagellar switching? As the flagellum likely evolved independently of the signaling network before the two became coupled, it is possible that the network's main function is other than chemotaxis. In which case, there is a possibility that chemotaxis is weak or absent in *C. crescentus*. In Chapter 5, we test this idea and investigate the link between flagellar dynamics of *C. crescentus* and biased migration towards attractants.

CHAPTER III PROTEIN EXPRESSION-INDEPENDENT RESPONSE OF INTENSITY-BASED PH-SENSITIVE FLUOROPHORES IN *ESCHERICHIA COLI**¹

Introduction

Flagellar rotation is driven by proton motive force (PMF), an electrochemical gradient maintained across the cell membrane, composed membrane potential and pH gradient [10]. The flagellar rotational speed was shown to vary linearly with PMF at high viscous loads [11]. The effect of membrane potential and pH gradient on the rotational speed has been tested by employing various techniques such as addition of ionophores or weak acids and using membrane dyes or fluorescent reporters to detect the change in the components of PMF [27, 46, 49, 73]. For example, in the presence of weak acids such as benzoate, the flagellar motor rotation is impaired upon a shift in external pH from 7.0 to 5.0 [74]. Because external pH can be altered, the intracellular pH must be accurately measured to calculate the pH gradient. Thus, there is a large interest in measuring intracellular pH with fast dynamics and high accuracy.

Bacteria maintain a tight control over their cytoplasmic pH even when the extracellular pH fluctuates significantly [75-79]. Homeostasis in the cytoplasmic pH is crucial for the regulation of important processes including enzymatic function, metabolism, ion channel activity, motility, and cell division [80-82]. Homeostasis is

¹ Rhee KY, Chawla R, Lele PP (2020) Protein expression-independent response of intensity-based pH-sensitive fluorophores in *Escherichia coli*. PLOS ONE 15(6): e0234849. <https://doi.org/10.1371/journal.pone.0234849>

promoted by several intrinsic buffering mechanisms including those that involve enzymatic systems including amino acid decarboxylases [5, 83-86], transcription factors [87, 88], ammonia-producing deaminase and deiminase systems [89], and ureases [90, 91]. Other mechanisms limit proton transport by modulating proton permeability of the phospholipid membranes and proton antiporter activity [5, 84, 92]. Gram-negative *Escherichia coli* are remarkable at maintaining pH homeostasis; their cytoplasmic pH ranges narrowly between 7.4-7.8 [31, 80, 93].

Intracellular pH has been traditionally measured with the aid of extracellular probes whose uptake by the cells is pH-dependent. Examples are membrane-permeant radiolabeled probes and fluorescent dyes [31, 94-96]. However, these approaches afford relatively low temporal and spatial resolution. Cell-cell variability in probe or dye uptake and leakage limit the accuracy of measurements [97]. The use of pH-sensitive fluorescent proteins helps circumvent these problems as the proteins are expressed intracellularly.

Several variants of the green fluorescent protein (GFP) have been developed that vary their emission intensities as a function of the ambient pH [98]. These so-called intensity-based probes exhibit two states that differ in the protonation state of the chromophore and that have distinct spectral characteristics [99]. Changes in the pH induce a shift in the equilibrium between the two states, thereby modulating the emission [100, 101]. Fluorescent proteins have become popular alternatives to traditional pH probes [102-104]. They have been widely employed in combination with spectroscopy, flow cytometry, and fluorescence microscopy [105, 106] to measure relative changes in pH with superior temporal and spatial resolution [107, 108].

The fluorescence signal is proportional to the number of fluorescent proteins expressed within each cell. In bacteria, cell-cell variability in the number of fluorophores can cause large fluctuations in the signal from intensity-based probes, especially given the tiny cell volumes. Fluorophore expression levels may also vary significantly across different mutant strains, complicating comparisons of their cytosolic pH. To overcome this key limitation of intensity-based probes, ratiometric fluorescent proteins such as pHluorin, GFP_H, and Rosella have been developed [32, 109-111]. Emissions are obtained under different excitation or emission settings, and ratios of the signals are then determined since they are independent of the expression levels of the fluorophores [112].

A key limitation in the use of the popular ratiometric probe, pHluorin, is that the illumination wavelengths used to excite the fluorophore cause the well-known blue light effect – incident light at 405 nm has bactericidal effects on a variety of species [113-117]. This could interfere with pH measurements by affecting cell physiology [116, 118]. Another problem is the need for multi-wavelength excitation setups, which can cost more and can prevent measurements of rapid changes in the pH, especially if the excitation wavelength must be repeatedly alternated.

Here, we explored whether pH-sensitive emissions from existing intensity-based fluorescent proteins could provide advantages similar to the ratiometric probes. We showed theoretically and experimentally how the emissions from Gfpmut3* and eYFP, two probes that excite at wavelengths where the blue light effect is diminished, can be made independent of the expression levels with a simple scaling analysis. The scaled signals were also independent of the photon excitation and detection settings. Therefore,

we propose that intensity-based probes can provide a robust method for detecting internal pH with appropriate scaling.

Materials and Methods

Cell culturing

All strains were derived from *E. coli* RP437 [119]. PCR-amplified fluorescent protein alleles were inserted into the MCS (multiple cloning sites) region of the pTrc99A vector to generate desired plasmids: pTrc99A-Gfpmut3*, pTrc99A-eyfp, and pTrc99A-pHluorin. DsRed-Express (pUC19 vector backbone) was obtained from Clontech (Cat. No. 632412) and transformed in pTrc99A. Overnight cultures were grown from isolated colonies in Tryptone broth (TB). Day cultures were grown from the overnight cultures (1:100 dilution) in 10 mL of fresh TB at 33°C. Ampicillin was added at a final concentration of 100 µg/mL to the overnight and day cultures. Expression levels of the fluorophores were controlled by adding 0 - 100 µM isopropyl β-D-1-thiogalactopyranoside (IPTG) to the day culture at the time of inoculation. The cultures were grown to an OD600 ~ 0.5 before washing three times via centrifugation (1500g, 5 min) in phosphate buffer (0.01M Phosphate buffer, 0.067 M NaCl, 10⁻⁴ M EDTA, 0.01M Sodium Lactate and 1 µM Methionine) [120, 121].

Modulation of intracellular pH

To measure changes in fluorophore emission intensities at varying pH, tunnel slides were prepared by sticking two glass surfaces together with double-sided adhesive

tapes. Approximately 30 μ l of 0.01% poly-L-lysine solution was introduced in the tunnel slide for \sim 5 min. It was subsequently exchanged with DI water or buffer by gently wicking the fluid from one end of the tunnel slide and adding \sim 7 times higher volume of the replacement fluid at the other end. This minimized the contact of the cells with poly-L-lysine. A concentrated cell suspension was then introduced and was allowed to stand for \sim 10 min to enable the cells to sediment and adhere to the coverslip. The unstuck cells were gently removed by wicking the fluid while adding buffer at the other end. The stuck cells were exposed to buffers of desired pH (5.0 to 9.0) containing 40 mM benzoate [105, 108, 122] for at least 5-10 min prior to the measurements.

Fluorescence assays

The live cells were imaged on a Nikon Ti-E microscope with a 60x water immersion objective (Nikon Instruments). The coverslip was scanned to select a region where the cell-coverage was dense and uniform (Figure III-1); regions with vacant areas were ignored. An LED illumination source (SOLA SE II 365 light engine, Lumencor) was used to excite the fluorophores. Emissions were collected from \sim 1000 cells at any instant (Figure III-1). Background correction was not deemed necessary since the coverslip contributed less than \sim 2% to the overall emission. Excitation and the emission signals were appropriately filtered depending on the fluorescent protein (see Table III-1). The emissions were relayed to a sensitive photomultiplier (H7421-40 SEL, Hamamatsu Corporation) and the photon-counts were recorded with custom-written LabView codes at a sample rate of 10 Hz for \sim 30 seconds. For pHluorin, 15 seconds of data was recorded

for each excitation wavelength: 410 nm and 475 nm. The illumination intensities from the light engine were attenuated such that the emissions always fell within the dynamic range of the photomultiplier. For each tunnel slide, emissions were recorded from four different regions. For each fluorophore, three biological replicates were carried out. For the representative pH-response shown in Figure III-1, a perfusion chamber was employed which enabled media to be exchanged.

Statistical testing

Two-tailed paired t-test was employed to determine statistical significance. Difference in mean intensities was considered significant for $p < 0.05$.

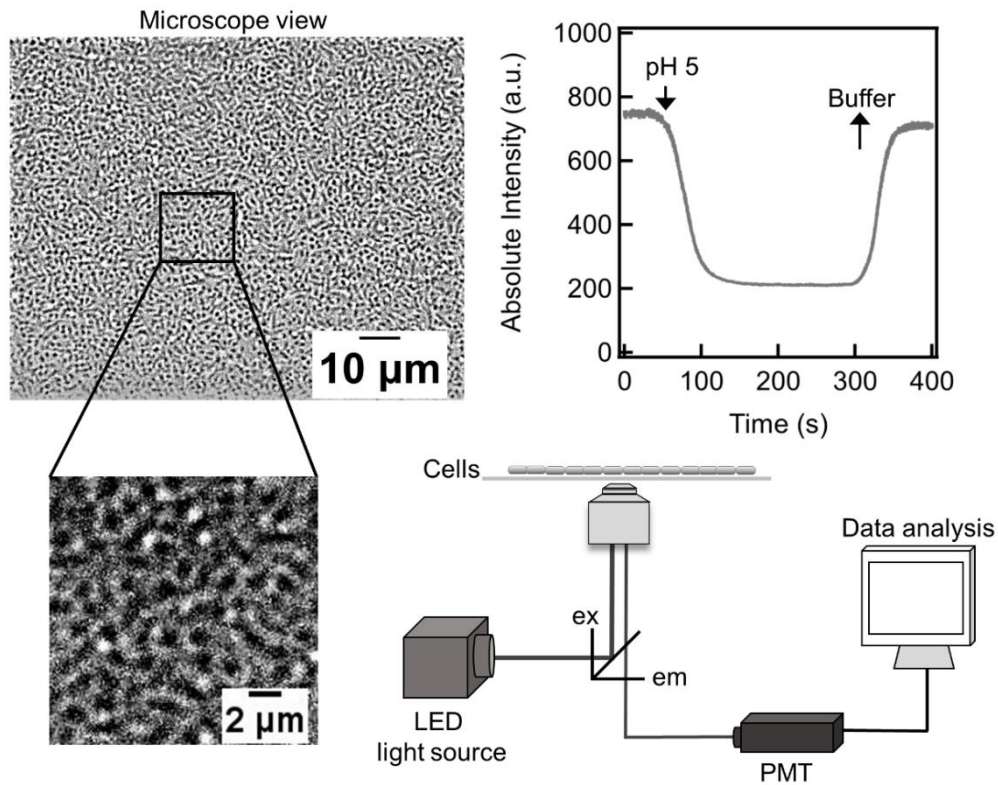


Figure III-1. Schematic of the experimental set-up.

A typical region of observation is shown (top left); inset shows a closer view of several cells stuck to the coverslip. White LED light was passed through a suitable excitation filter (ex) before illuminating the sample. The emissions were filtered with an emission filter (em) and relayed to a photon-counting photomultiplier (bottom right). Time-varying emissions from Gfpmut3* containing cells is shown (top right). The neutral buffer was exchanged with an acidic medium containing benzoate at ~ 50 s. A sharp reduction in intensity was observed in real-time. The original buffer was re-introduced at ~ 300 s, following which the intensity returned to its pre-stimulus value (after accounting for photobleaching). The calculated statistical power for this response was ~ 1.

Table III-1. Filter information

Fluorescent protein	Excitation	Emission
eYFP	Zet514/10x [†]	FF01-542/27 [*]
Gfpmut3 [*]	FF01-466/40x [*]	FF03-525/50x [*]
pHluorin	FF01-466/40x [*] FF01-409/32-25 [*]	FF03-525/50x [*]
DsRed-Express	FF01-542/22 [*]	FF01-598/25 [*]

[†] - Chroma Tech Corp. ^{*} - Semrock Inc.

Results

pH-sensitive fluorophore emission

We separately expressed Gfpmut3^{*}, eYFP, and pHluorin in *E. coli* from a common, inducible expression vector. Cells were stuck to poly-L-lysine coated coverslips in tunnel slides and their fluorescence emissions were measured with a photomultiplier. To measure emissions over a range of intracellular pH, cells were treated with 40 mM benzoate in phosphate buffers maintained at specific pH values (see Materials and Methods). In its protonated form, benzoate permeates the membrane and equalizes the cytoplasmic and extracellular pH [105, 108].

Gfpmut3^{*} and eYFP are intensity-based fluorophores, where the excitations and emissions of interest occur over single wavelengths (Table III-1). The absolute emission intensities of Gfpmut3^{*} and eYFP over varying pH are shown in Figure III-2A. The intensities were the lowest at pH 5.0 and increased with pH before plateauing for pH

values > 7.0 . Three induction levels were tested for each type of fluorophore: basal or low expression ($0 \mu\text{M}$ IPTG), medium expression ($10 \mu\text{M}$ IPTG) and high expression levels ($100 \mu\text{M}$ IPTG). The emission intensities increased with protein expression levels (Figure III-6). Hence, the illumination intensity was appropriately attenuated to operate within the working range of our photomultiplier detection system. Both fluorophores showed similar trends with respect to the internal pH.

pHluorin displays a dual excitation peak at 410 nm and 475 nm with a common emission at a wavelength of 509 nm [32]. Therefore, two excitation wavelengths were employed to measure the pH-sensitive signals from this fluorophore. The emission ratio was calculated by dividing the emissions at the lower excitation wavelength by the emissions at the higher excitation wavelength. The emission ratios versus internal pH for pHluorin are shown in Figure III-2B for the three expression levels. The dependence of the ratios on the pH was qualitatively similar to the emission curves obtained for Gfpmut3* and eYFP. At the highest induction level studied, pH-induced changes in the signals of Gfpmut3* (and of pHluorin) were statistically significant until pH 8; changes in the signals of eYFP were significant until pH 6. This suggests that Gfpmut3* is effective in detecting $\Delta\text{pH} = 1$ over the range of pH 5 to 8. At the basal expression level ($0 \mu\text{M}$ IPTG), pH-induced changes in the signals were not significant for the three fluorophores.

In contrast to the three pH-probes, a pH-insensitive protein, DsRed-Express, exhibited constant emission values over the pH range at $100 \mu\text{M}$ expression (Figure III-7), in agreement with prior reports [123].

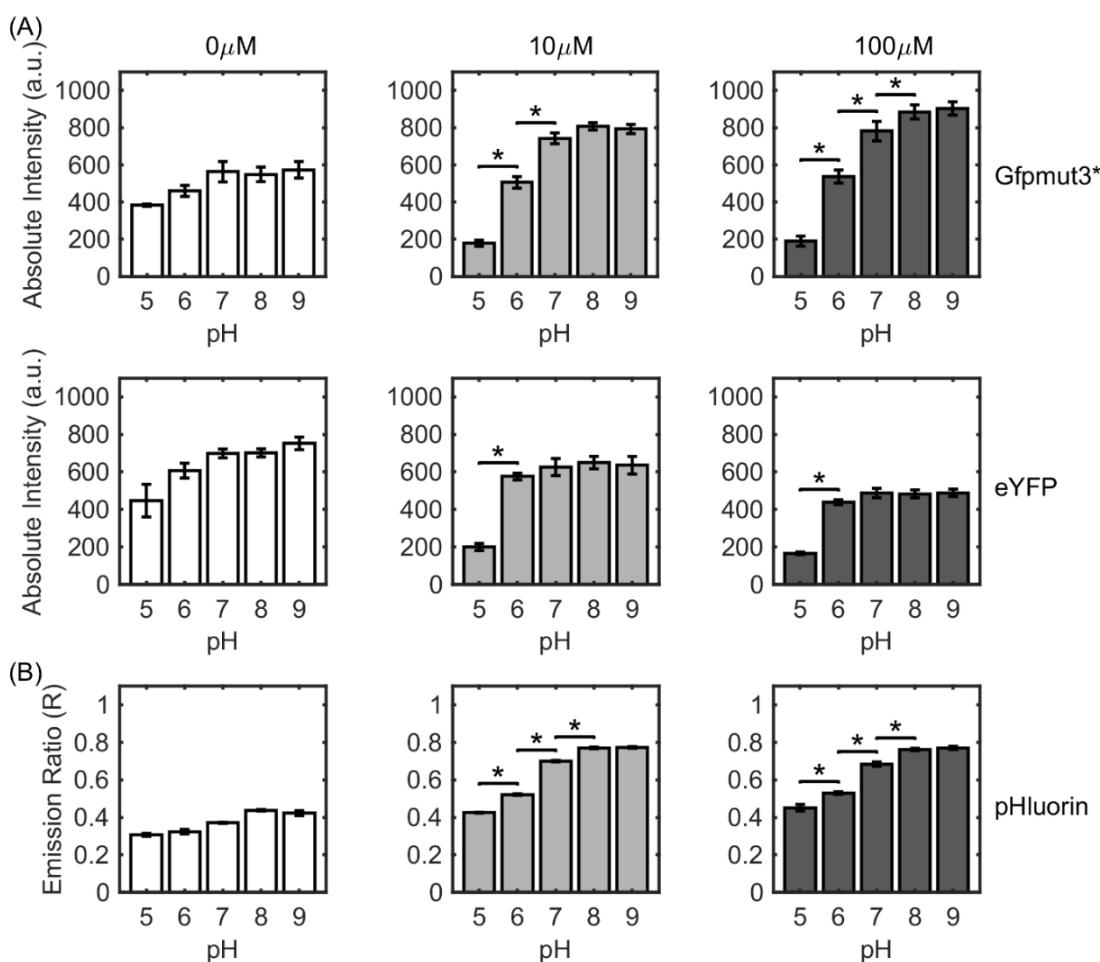


Figure III-2. pH-sensitive emission intensities for fluorophores.

A) Absolute intensities are indicated over a range of cytoplasmic pH values for Gfpmut3* (top row) and eYFP (bottom row). B) The ratios of emissions at two excitation wavelengths for pHluorin are shown as a function of cytoplasmic pH. Induction levels (IPTG concentrations) were 0 μM (white bars), 10 μM (light gray), and 100 μM (dark gray). Since the absolute intensities for all three fluorophores increased with the induction levels, the illumination intensity was attenuated as needed to operate within the dynamic range of our photomultiplier. Each data point reflects the mean value determined from four technical and three biological replicates ($n \sim 10,000$ cells). Standard error was estimated from the biological replicates; * indicates $p\text{-value} < 0.05$.

Analytical model to eliminate dependence of signals on expression levels

For intensity-based pH probes, the total emission intensity (I^{cell}) from each cell can be represented as a sum of the emissions from the protonated, N_{prot} , and the deprotonated, $(N - N_{prot})$, subpopulations.

$$I^{cell} = (N - N_{prot})I_{deprot} + N_{prot}I_{prot} \quad \text{III-1}$$

N is the total fluorophore population. I_{prot} and I_{deprot} refer to the emission intensities of individual protonated and the deprotonated fluorophores. The emission from the protonated fluorophore is lower than the deprotonated fluorophore ($I_{prot} < I_{deprot}$). We assume that there are no interactions between the fluorophores.

The fraction of the protonated fluorophores within the cell is assumed to be in equilibrium with the proton abundances within the cell, $[H^+]_{in}$:

$$\frac{N_{prot}}{N} = \frac{[H^+]_{in}}{K + [H^+]_{in}} \quad \text{III-2}$$

Here, K is the dissociation constant which depends on the type of the fluorophore. Equation III-2 is a reasonable assumption since the cell has a considerable buffering capacity and carries millions of ionizable groups that are more abundant than the fluorophores. The proton abundance was estimated from the internal pH as per the relation:

$$[H^+]_{in} = 10^{-pH} * N_A * V_{E. coli} \quad \text{III-3}$$

N_A is the Avogadro's number, and $V_{E.coli}$ is the cytoplasmic volume of *E. coli*.

As is evident from Equations III-1 to III-3, the signal from each cell is dependent on the fluorophore intensities (I_{prot} and I_{deprot}), the fluorophore expression levels (N), and

K. A key outcome from the model is that when the intensity is scaled (min-max normalization), the scaled intensity (\hat{I}) becomes independent of the emission intensities altogether (see Supplementary equations 1):

$$\hat{I}^{cell} = \frac{I^{cell} - I_{min}^{cell}}{I_{max}^{cell} - I_{min}^{cell}} = \frac{(N_{prot}^{pH\ min} - N_{prot}^{pH})}{(N_{prot}^{pH\ min} - N_{prot}^{pH\ max})} \quad \text{III-4}$$

This is convenient since it theoretically eliminates variations associated with the differences in illumination sources, detector gain and filters among other factors.

The scaled or normalized intensity at a given pH can be further shown to depend solely on K and the minimum pH value employed in the normalization. Since the difference in the maximum and minimum pH values chosen in our work is large (9 and 5, respectively), the condition $N_{prot}^{pH\ min} \gg N_{prot}^{pH\ max}$ is satisfied for most fluorescent proteins (pKa values $\lesssim 7.0$).

$$\therefore \hat{I}^{cell} \sim 1 - \frac{\left(1 + \frac{K}{[H^+]_{in}^{pH\ min}}\right)}{\left(1 + \frac{K}{[H^+]_{in}}\right)} \quad \text{III-5}$$

Equation III-5 indicates that the scaled intensities are independent of the expression levels of intensity-based fluorescent proteins, such as GFP and YFP. Finally, it is straightforward to prove that $\hat{I}^{cell} = \hat{I}$, where \hat{I} is the mean scaled intensity for a population of cells.

Having demonstrated that the scaling analysis makes the signals from an intensity-based fluorophore independent of the absolute values of the fluorophore emissions and the expression levels, we tested it experimentally. According to the model, the scaling should

cause the experimental curves to collapse onto standard curves for Gfpmut3* and eYFP. The equivalence between the mean normalized intensity of a population of cells and the normalized single-cell level output meant that we could simply scale the data in Figure III-2 to test the prediction. Indeed, the normalized curves were superimposable as shown in Figure III-3A, even though the protein expression at different induction levels was clearly different (Figure III-6). Equation 5 was then fitted to the experimental data with a single parameter, K , using Levenberg-Marquardt algorithm for iterative curve fitting (Igor Pro 7). For Gfpmut3*, a common fit was obtained since the normalized data at all expression levels coincided with each other. For eYFP, a good fit was obtained for the cases of the medium and high fluorophore expression levels (inducer IPTG concentrations of 10 and 100 μM). At low (basal) expression levels of eYFP, the experimental curve deviated from the standard curve. This was likely because of poor signal-noise ratio due to the paucity of fluorophores. The value of K for Gfpmut3* was an order of magnitude lower than that for eYFP. This is consistent with the higher pKa values reported for eYFP relative to some GFP variants [124].

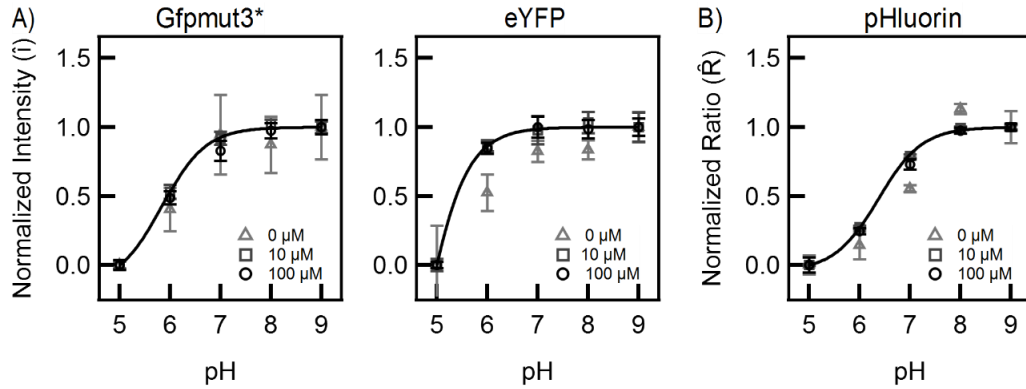


Figure III-3. Normalized emission intensities and ratios as a function of cytoplasmic pH.

A) Normalized curves for Gfpmut3* (left panel) collapsed onto a single curve for the different expression levels. For eYFP (right panel), the data collapsed on a single curve with the exception of the low or basal expression level (0 μM IPTG, Δ). The solid curves represent fits with equation 5 with a single fit parameter, K . $K = (1.8 \pm 0.13) \times 10^3$ protons for Gfpmut3*; $K = (2.9 \pm 1.4) \times 10^4$ protons for eYFP. B) The normalized emission ratios over a range of pH for pHluorin are indicated. The solid curve represents fits with equation 5; $K = 540 \pm 24$ protons.

Dependence of ratiometric emission ratios on illumination and detection conditions

From Equation III-1, the ratio of the emissions for a dual excitation fluorescent protein can be expressed as:

$$R(pH) = \frac{I_{prot}^2}{I_{prot}^1} \times \frac{(N - N_{prot})\delta_2 + N_{prot}}{(N - N_{prot})\delta_1 + N_{prot}} \quad \text{III-6}$$

A similar ratio can be written for the case of dual-emission proteins with minor modifications. The emission intensity of the deprotonated pHluorin is represented by I_{unprot}^1 at the higher excitation wavelength and I_{unprot}^2 at the lower excitation wavelength. The emission intensity of protonated pHluorin is represented by I_{prot}^1 at the higher excitation wavelength and I_{prot}^2 at the lower wavelength. Also, the relative intensities at

the two wavelengths are: $\delta_1 = \frac{I_{unprot}^1}{I_{prot}^1}$ and $\delta_2 = \frac{I_{unprot}^2}{I_{prot}^2}$. The relation expectedly simplifies

to an expression that is independent of the protein levels:

$$R(pH) = \frac{I_{prot}^2}{I_{prot}^1} \times \frac{([H^+]_{in} + K\delta_2)}{([H^+]_{in} + K\delta_1)} \quad \text{III-7}$$

Equation III-7 suggests that the ratio R will be sensitive to changes in the pH only if $\delta_2 \neq \delta_1$. Thus, ratiometric proteins are only useful for pH measurements if the relative intensities at the two wavelengths are unequal. Since δ_2 and δ_1 are influenced by several factors associated with the illumination and detector setup, such dependencies are undesirable.

We explored whether a min-max normalization could make the ratios independent of the emission intensities and the expression levels for pHluorin. As shown in Supplementary equations 2, the scaling yielded an expression very similar to Equation III-5:

$$\hat{R}(pH) = 1 - \frac{\left(1 + \frac{K}{[H^+]_{in}^{pH \min}}\right)}{\left(1 + \frac{K}{[H^+]_{in}}\right)} \beta \quad \text{III-8}$$

where $\beta = \frac{1}{1 + \omega \frac{[H^+]_{in}}{(K + [H^+]_{in})}}$ and $\omega = \left(\frac{1}{\delta_1} - 1\right)$.

Since β depends on the relative emission intensities at the higher excitation wavelength, it is interesting to note that the experimental ratios for different expression levels collapsed on a single curve for pHluorin (Figure III-3B). This suggests that the experimental \hat{R} is only weakly dependent on β . Consistent with this notion, good fits were

obtained for the normalized pHluorin emission ratios with Equation III-5 (Figure III-3B). The value of K for pHluorin was the lowest among the three fluorophores.

Dynamic range and sensitivity of intensity-based probes

The dynamic range for a pH-sensitive fluorophore is defined as the highest emission intensity divided by the lowest intensity [125]. It is a useful quantity in choosing an appropriate pH-sensitive fluorophore to improve accuracy. Fluorophores with dynamic range ~ 1 are unsuitable probes due to low statistical power. The dynamic range was calculated for Gfpmut3* and eYFP at the three expression levels (Figure III-4). The range was optimal for the medium expression and the high expression levels; it was the lowest at basal expression levels due to poor signal-to-noise ratios. Gfpmut3* exhibited a higher range than eYFP on our setup and for the strain of *E. coli* that we used.

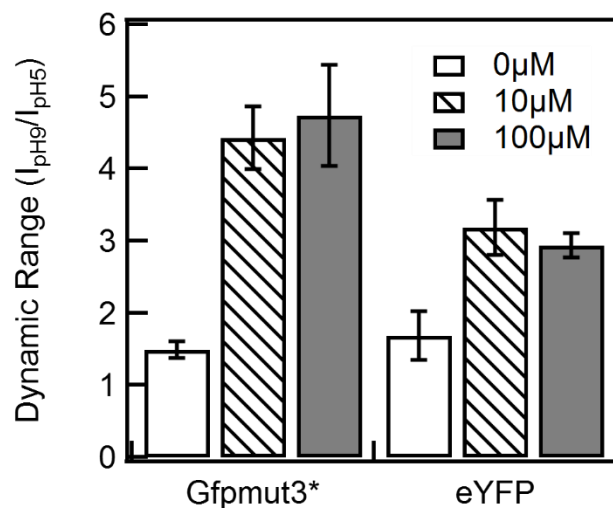


Figure III-4. Dynamic range in pH measurements.

Dynamic ranges are shown for the intensity-based probes: dynamic range is the emission intensity at pH 9 (I_{pH9}) divided by the intensity at pH 5 (I_{pH5}). Induction levels are indicated in the figure legend. Error bars were determined by error propagation.

Fluorophore sensitivity is another characteristic of interest when choosing fluorophores. Experimental sensitivities were calculated at the medium expression level (10 μ M IPTG) since it provides a good dynamic range and is similar to the response at the high expression level (Figure III-5). The predicted sensitivity curves were obtained by differentiating Equation III-5. As shown in Figure III-5, the experimental data and the predicted curves are in close agreement. Among the three fluorophores, eYFP is the most sensitive and exhibited high sensitivities at lower pH values (\sim 5.0). Over physiological values of the intracellular pH though, eYFP had a low sensitivity. Thus eYFP is a suitable probe for the dynamics of protein self-assembly in live bacteria at physiological pH, since sensitivity to pH can confound results and interpretation [126-128]. Gfpmut3* and

pHluorin exhibited similar sensitivities and the peaks in sensitivities occurred over a narrow range of pH (6.0-6.5).

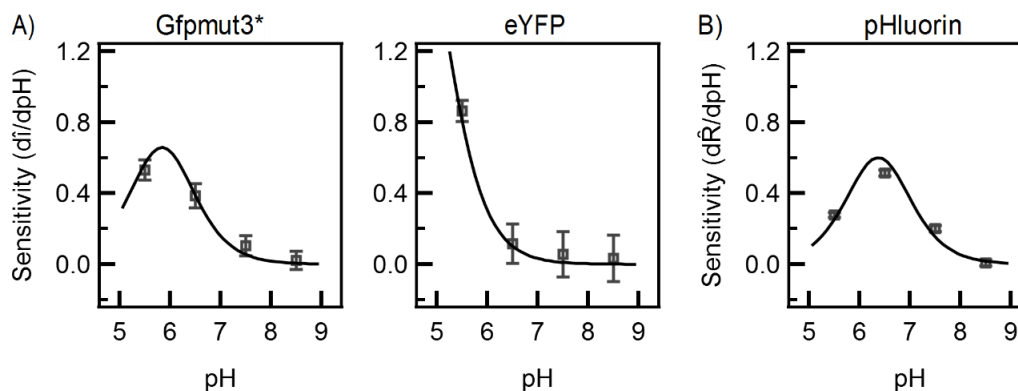


Figure III-5. Fluorophore sensitivity versus pH.

The experimental sensitivities (indicated by symbols) were calculated for the medium expression level case (10 μ M IPTG) for each type of fluorescent protein. The solid lines indicate model predictions based on the fitted K-values for the respective fluorophores from Fig 3. eYFP exhibited the highest sensitivity among the three fluorescent proteins. Gfpmut3* and pHluorin exhibited similar sensitivities and peaked between pH 6.0 - 6.5. Error bars were determined by error propagation.

Discussion

A two-state analytical model was developed to interpret the pH-sensitive response of intensity-based and ratiometric fluorophores. We assumed two emission states for each fluorophore: a low intensity protonated state and a high intensity deprotonated state. We also assumed that the fluorophore concentration did not affect the proton abundances in the cell – the protonated fluorophore fraction was always in equilibrium with the cytoplasmic protons. The model suggested a simple scaling to render the emissions from intensity-based fluorescent proteins independent of the fluorophore expression levels.

This was true for single cells as well as for a population. The predicted independence of the scaled signals was experimentally confirmed for Gfpmut3* and eYFP over the range of pH 5 – 9. .

The scaling analysis also suggested that the normalized signals from intensity-based fluorophores were independent of the absolute emission intensities of the protonated and deprotonated fluorophore. This is advantageous since it potentially eliminates the influence of experimental variabilities in illumination intensities, detector gain, and the differences in the optics used in different laboratories.

The value of K quantified the tendency of the fluorophore to protonate at a given pH. It shaped the non-linear emission curves, leading to a characteristic rise and plateauing observed for all three fluorescent proteins (Figure III-2). The scaled signals from intensity-based probes were predicted to depend solely on K . Therefore, in principle, an intensity measurement can help determine the internal pH of a single cell (or a population of cells) from the knowledge of just the minimum and maximum intensities (i.e, intensities at pH 5 and pH 9). The value of K was ~ 20 times higher for eYFP compared to pHluorin in the strains that we employed here. In addition to depending on the chromophore type and the bacterial species, K is likely to be impacted by environmental stressors and cell metabolism.

We extended the model to analyze the emissions from ratiometric probes. The signal was dependent on the emission intensities of the fluorophores - simple scaling could not eliminate this dependence. But, rigorous calibration can help address this problem even if the illumination/detection conditions were to change. The sensitivity of the

emission ratios to the pH was predicted to be due to the difference in δ_1 and δ_2 : these are the ratios of the emission intensities of the deprotonated and protonated fluorophore at the two excitation wavelengths (see Equation III-7). For $\delta_1 = \delta_2$, the emission ratio will remain insensitive to pH. We recommend that this criterion be adopted for designing ratiometric probes.

The suitability of a probe for pH detection is determined not only by the intrinsic noise in measurements, but also by its sensitivity to pH fluctuations and the dynamic range. eYFP exhibited the highest sensitivity (at pH ~ 5) and dropped sharply at higher pH values. Thus, eYFP is a suitable probe under acidic conditions. Since Gfpmut3* and pHluorin exhibited similar sensitivities that peaked around ~ pH 6.0, the latter is more reliable in detecting small changes in the pH due to the lower noise associated with its emission ratios. Gfpmut3* displayed a higher dynamic range than eYFP, which translates to a superior signal-to-noise ratio. Induction from the *pTrc99A* vector with 10 μ M IPTG was determined to be optimal since it provided the best dynamic range, sensitivities and signal-noise ratios. Higher expression levels of the chimeric proteins may cause unwanted effects such as the formation of inclusion bodies and increased toxicity [129] and thus, should be avoided. In the absence of the inducer, the basal expression (~ 1000 fluorophores) was too low to obtain reliable measurements [130].

Several types of intensity-based as well as ratiometric fluorophores are available that can be excited at higher wavelengths to avoid the blue light effect [104, 109-111]. However, intensity-based fluorophores require simpler setups (single wavelength excitation and emission), which allows rapid sampling of short-time dynamics (Figure

III-1). We anticipate that our analysis and experiments will help extend the applications of intensity-based pH reporters for pH-sensitive measurements and provide a useful guide for the selection and the use of appropriate fluorescent probes.

Supplementary Information

Supplementary figures

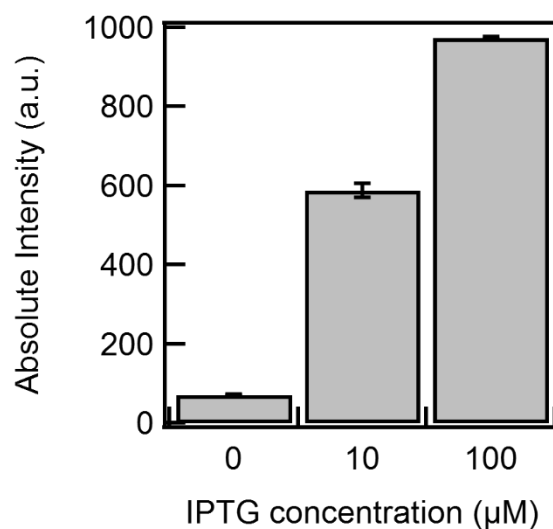


Figure III-6. Relative expression levels of Gfpmut3* at different IPTG concentrations.

Absolute intensities in live cells were obtained over three induction levels of Gfpmut3*. The same illumination intensities and detection settings were used for all three datasets. Mean values are from four technical replicates; standard error is indicated. Differences in intensities between 0 and 10 μM , and between 10 and 100 μM were statistically significant (p -value < 0.05).

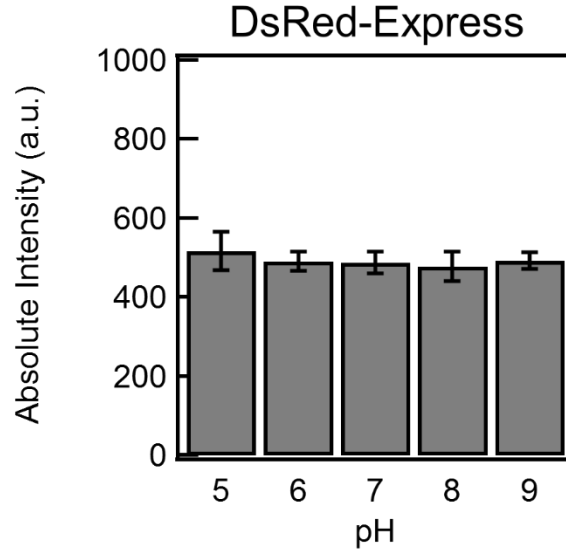


Figure III-7. Emissions from pH-insensitive DsRed-Express.

DsRed-Express was expressed with 100 μ M IPTG. Each mean value was calculated from four technical and three biological replicates. Standard error is indicated based on the biological replicates. A two-tailed, paired t-test was performed to compare each adjacent pair. Differences in means were insignificant (p-value > 0.05).

Supplementary equations 1

The maximum and minimum emission intensities are defined at pH_{max} and pH_{min} ,

which indicate the range of experimental conditions:

$$I_{\text{max}}^{\text{cell}} = N_{\text{prot}}^{\text{pH max}} I_{\text{prot}} + (N - N_{\text{prot}}^{\text{pH max}}) I_{\text{unprot}} \quad (\text{a})$$

$$I_{\text{min}}^{\text{cell}} = N_{\text{prot}}^{\text{pH min}} I_{\text{prot}} + (N - N_{\text{prot}}^{\text{pH min}}) I_{\text{unprot}} \quad (\text{b})$$

$$\Delta I = I_{\text{max}}^{\text{cell}} - I_{\text{min}}^{\text{cell}}$$

$$= (N_{\text{prot}}^{\text{pH min}} - N_{\text{prot}}^{\text{pH max}}) I_{\text{prot}} (\delta - 1) \quad (\text{c})$$

where, $\delta = I_{\text{unprot}}/I_{\text{prot}}$

$$f^{\text{cell}} = \frac{I_{\text{max}}^{\text{cell}} - I_{\text{min}}^{\text{cell}}}{\Delta I}$$

$$= (N_{prot}^{pH\ min} - N_{prot}^{pH}) / (N_{prot}^{pH\ min} - N_{prot}^{pH\ max}) \quad (d)$$

When $pH\ min$ and $pH\ max$ are separated by several orders of magnitude, the expression reduces to:

$$= (1 - N_{prot}^{pH} / N_{prot}^{pH\ min}) \quad (e)$$

Thus, the normalized intensities $\hat{I}(pH)$ are independent of the differences in the absolute intensities of the protonated and the deprotonated states of the fluorophore.

Supplementary equations 2

$$R(pH) = \frac{I_{prot}^2}{I_{prot}^1} \times \frac{(N - N_{prot})\delta_2 + N_{prot}}{(N - N_{prot})\delta_1 + N_{prot}} \quad (f)$$

$$\begin{aligned} \hat{R}(pH) &= \frac{R(pH) - R_{min}}{R_{max} - R_{min}} \\ &= \frac{(N_{prot}^{pH\ min} - N_{prot}^{pH})}{(N_{prot}^{pH\ min} - N_{prot}^{pH\ max})} \frac{(N - N_{prot}^{pH\ max})\delta_1 + N_{prot}^{pH\ max}}{(N - N_{prot})\delta_1 + N_{prot}} \end{aligned} \quad (g)$$

$$[H^+]_{in}^{pH\ max=9} \sim 1, \therefore N_{prot}^{pH\ max} \ll N,$$

$$\begin{aligned} \hat{R}(pH) &\sim \frac{(N_{prot}^{pH\ min} - N_{prot}^{pH})}{(N_{prot}^{pH\ min} - N_{prot}^{pH\ max})} \frac{N\delta_1}{(N - N_{prot})\delta_1 + N_{prot}} \\ &\rightarrow \delta_1 = \frac{I_{unprot}^1}{I_{prot}^1} \end{aligned} \quad (h)$$

$$\hat{R}(pH) \sim \frac{(N_{prot}^{pH\ min} - N_{prot}^{pH})}{(N_{prot}^{pH\ min} - N_{prot}^{pH\ max})} \frac{1}{1 + N_{prot}(1/\delta_1 - 1)/N} \quad (i)$$

$$\hat{R}(pH) \sim \frac{(N_{prot}^{pH\ min} - N_{prot}^{pH})}{(N_{prot}^{pH\ min} - N_{prot}^{pH\ max})} \frac{1}{1 + \frac{K[H^+]_{in}}{(K + [H^+]_{in})}\omega} \quad (j)$$

where, $\omega = \frac{1}{N} \left(\frac{1}{\delta_1} - 1 \right)$.

CHAPTER IV RELATION BETWEEN THE PROTON MOTIVE FORCE,
SWIMMING SPEEDS AND FLAGELLAR ROTATION RATES IN MULTI-
FLAGELLATED BACTERIA

Introduction

As previously discussed in Chapter II and Chapter III, there are many available techniques to measure the membrane potential and intracellular pH in bacteria. Most methods involve fluorescence microscopy, which makes it difficult to measure both components simultaneously. Because both membrane potential and pH gradient contribute significantly to the total PMF, it is crucial to measure the PMF itself [28, 29]. To probe PMF, we can take advantage of processes that are powered by the PMF.

One of the processes powered by the PMF in *E. coli* is the bacterial flagellar motor. Protons are transported across the stator complex, made up of MotA and MotB, which generates torque to rotate the flagellar motor. The motor is connected to the flagellar filament with the hook. The hook is a universal joint and the filament generates propulsive force [131]. The relationship between the flagellar rotation speed and PMF has been quantitatively measured by the Berg lab. In their study, the PMF was tuned with ionophores such as gramicidin S or carbonyl cyanide 3-chlorophenylhydrazone (CCCP). The flagellar rotation speed of *E. coli* was measured using the tethered cell and the bead assay. Their work indicated that the flagellar rotation speed is linearly proportional to the PMF in *E. coli* [11, 45]. Thus, it is possible to estimate the PMF from flagellar speeds in this bacterial species.

Flagellar assays have been developed in only a handful of other bacterial species. However, swimming speeds are straightforward to measure in all bacterial species. Is there a predictable correspondence between the swimming speed, flagellar speeds, and the PMF? If yes, the PMF could be readily predicted from changes in the swimming speeds alone, circumventing the need for complicated flagellar probes. In this work, we attempted to describe the relationship between the PMF, the flagellar rotation rates and the swimming speeds in *B. subtilis*. This was a convenient choice as *B. subtilis* is a model species and probes for flagellar behavior have already been developed [50, 132].

One complication in *B. subtilis* is that the flagellar motors may not be powered solely by the PMF but also by the SMF (sodium motive force). There are two stator complexes that interact with the motor: MotAB powered by H⁺ and MotPS powered by Na⁺. During swimming, the dominant stator complex is the MotAB since deletion of the MotPS complex does not affect the swimming speed [52, 54]. However, the role of MotPS is dependent on the Na⁺ concentration, pH, and load [50, 51]. In the neutral motility buffers that we have used, MotPS are not known to contribute much to the motor torque.

As we will elaborate, we measured the flagellar rotation speeds in swimming cells in *E. coli* and *B. subtilis* using fluorescence microscopy. *B. subtilis* rotated 30% slower compared to *E. coli*. We hypothesized that similar difference would be observed in their swimming speeds. Surprisingly, the two species swam at similar speeds. This confirmed that flagellar rotation rates and swimming speeds are heavily influenced by hydrodynamic factors. A simple hydrodynamic model that accounted for these factors was insufficient in resolving the discrepancy between the swimming speed and rotational speeds. This meant

that changes in the flagellar rotation rates (and PMF) cannot simply be predicted from the swimming speeds in peritrichous species. To address this problem, we prepared a plot of the membrane potential vs. swimming speeds in *B. subtilis*. This plot will serve as a reference for estimating changes in the PMF from swimming speeds in this species in the future.

Materials and Methods

Strains and media

All strains are listed in Table S1. *B. subtilis* strains were a gift from Dave Dubnau and are derived from the laboratory wild type strain IS75, a derivative of strain 168. *E. coli* strains are derived from RP437 or AW405 parent strain. Overnight cultures were grown from isolated colonies in TB media (10 g/L Tryptone and 5 g/L NaCl) at 30°C for *E. coli* and LB media (10 g/L Tryptone, 5 g/L NaCl, and 5 g/L Yeast Extract) at 37°C for *B. subtilis*. Day cultures were grown by diluting 100 µL of overnight culture in 10 mL of TB media at 33°C to OD₆₀₀~0.5 for *E. coli* and in 10 mL of LB media at 37°C OD₆₀₀~1 for *B. subtilis*. Antibiotics (100 µg/mL of ampicillin for *E. coli*; 5 µg/mL of chloramphenicol, 25 µg/mL of tetracycline, and 1 µg/mL of erythromycin for *B. subtilis*) were added when needed. Motility buffer (MB) (0.01 M Phosphate buffer, 0.067 M NaCl, 10⁻⁴ M EDTA, 0.01 M Sodium Lactate, and 1 µM Methionine, pH ~ 7.0) was employed in motility assays.

Swimming speed and cell size

B. subtilis cells were washed very gently twice in MB via low centrifugation (1000 g, 7 minutes), with care taken to not shear the flagellar filaments. Cells were diluted in

MB (1:10 dilution) and observed on a standard flow cell. The cell motion was imaged and recorded with a 20x objective with a CMOS camera (UI-3240LE-M-GL). The video was analyzed using a custom written particle tracking algorithm in Matlab to determine the swimming speed and the cell size. In PMF dissipation experiments, cells were suspended in MB supplemented at different concentrations of CCCP for five minutes before recording their motility.

Hook and filament fluorescent labeling

A cysteine mutation on a surface-exposed residue enables fluorescent labeling of the hook or the filament. The appropriate strain for hook and filament labeling was used (Table S1). Cells were grown to the desired OD, washed in MB, gently resuspended in a final concentration of 60 mM Atto 514 maleimide dye. The falcon tube containing the stained cells was always covered with aluminum foil to prevent photobleaching. The tube was gently shaken for 45 minutes at 70 rpm for labeling. After labeling, cells were gently washed twice to remove excess dye using MB and resuspended in 3 mL fresh MB. For double filament labeling, cells were instead resuspended in 5 mL of LB and was grown for additional hour at 37°C. Cells were removed from the growth media and the newly grown filaments were labeled as described previously with 60 mM Alexa Fluor 647 maleimide dye.

To visualize the cells, a standard flow cell treated with 0.01% poly-L-lysine was used to stick the cells down. However, all of the filaments in *B. subtilis* did not adhere to poly-L-lysine coated slide due to the high number of motors. To resolve this, cells were

inoculated on a thin LB agar pad and a coverslip was placed on top of the cells, gently not to shear the filaments away. All cells were visualized under the microscope (Nikon Eclipse Ti-E) with a 60x water objective with a CCD camera (Andor Zyla). A white LED light (SOLA LE engine) was passed through bandpass filters for respective maleimide dye to obtain filament fluorescence images.

The images of fluorescent hooks and filaments were processed in ImageJ and number was manually counted. To analyze the filament geometry, a custom written Matlab code was utilized. An intensity profile of the helical filament was determined by drawing a line across the centerline of the filament, and it was filtered through Fourier transform to calculate the pitch length. The amplitude was calculated by measuring the length between the top and the bottom of the helix. Lastly, the arc length was determined by inputting the endpoints of the filament.

Flagellar rotation rate

Flagellar filaments were stained with maleimide dye as previously described. In order to observe motility in *B. subtilis*, the cells were re-energized in LB. Cells were visualized under a Nikon Ti-E microscope with a 60x oil objective with an Andor iXon DU897 camera. To capture TIRF (total internal reflection fluorescence) images, a 100 mW, 514 nm laser beam (Cobalt Fandango) was focus to create evanescent fields. The images were taken at 500 frames per second with an exposure time of 0.0001 s in batches of 100 frames. The images were processed in ImageJ, the number of frames taken for a full rotation was manually counted to determine the rotation rate.

Membrane potential measurements

After cells were washed in MB, the final wash was conducted in MB supplemented with 10 μ M of Thioflavin T (ThT). Cells were concentrated and attached to a 0.01% (w/v) poly-L-lysine coated coverslip. Cells were loaded on a perfusion chamber and imaged with a Nikon Ti-E microscope with a 60x water immersion objective. To obtain ThT signals, LED light from SOLA LE engine was passed through a 435/20 nm excitation filter and collected with an emission filter 525/50 nm. The signal was relayed to a sensitive photomultiplier (Hamamatsu) with a sampling rate of 10 Hz. The cells were continually perfused with either MB-ThT solution or MB-ThT solution supplemented with CCCP.

Results

Flagellar rotational speed

Two species of peritrichous bacteria Gram-negative *E. coli* and Gram-positive *B. subtilis*, were chosen as the subject of study as they are both easy to genetically modify motile species with established flagellar motor assays. The flagellar rotation rate was measured by visualizing swimming cells with fluorescently labeled flagella with total internal reflectance fluorescence microscopy (TIRF) at a high frames per second (fps). A fps of 500 was chosen since the flagellar bundle rotation rate of *E. coli* is known to be around 130 Hz [133]. A snapshot of the single flagellar bundle is shown in Figure IV-1. Because TIRF only illuminates 200 nm from the surface, we can only observe the bottom slice of the helical filament. Using image analysis, we determined the rotation rate by

counting the number of frames it took for a full rotation. The flagellar rotation rate for *B. subtilis* was lower by 31.8% compared to *E. coli* (Figure IV-1).

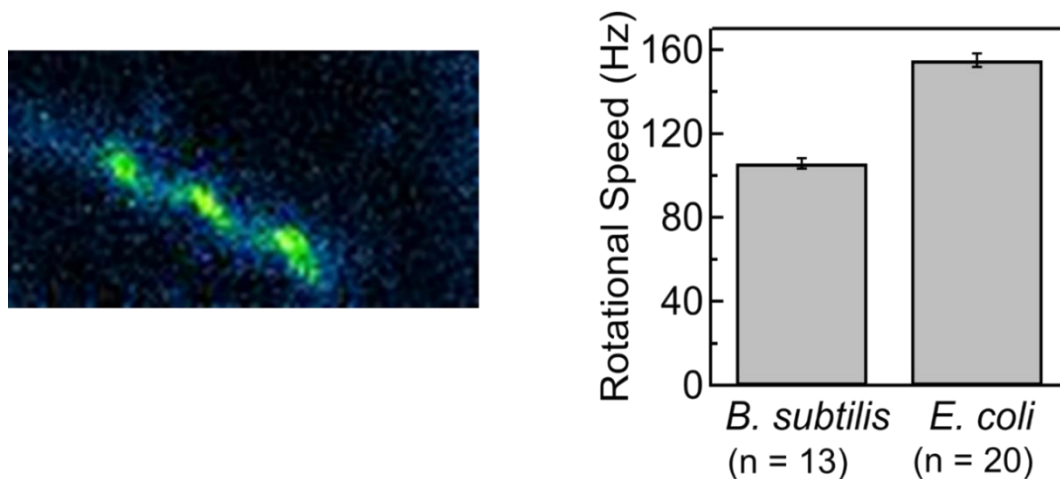


Figure IV-1. Motor rotational speed measurements for *E. coli* and *B. subtilis*. Fluorescently-labeled flagella of swimming cells were imaged at 500 fps with an EMCCD camera. The rotational speed of the two species were analyzed using image analysis. The error bars indicate standard errors.

Swimming speed and cell length

The swimming speed is proportional to the flagellar rotation rate, as described by the propulsive matrix [131]. Therefore, we hypothesized that *B. subtilis* cells should swim at a slower speed than *E. coli*. Videos of swimming bacteria in a dilute suspension of MB were recorded (see Materials and Methods). Particle tracking analysis was employed to determine the individual swimming speeds along with the cell geometry. Deviating from our hypothesis, no significant difference in the mean swimming speeds was measured between the two species (Figure IV-2). Therefore, we sought to determine various cell

parameters to understand the discrepancy between flagellar rotation rate and swimming speed.

One of the cell parameters that affect swimming speed is the cell geometry. Longer cells induce a higher drag force experienced by the cell, which could lower the swimming speed [134]. As shown in Figure IV-2, *B. subtilis* cells were longer than *E. coli* by three-fold, which suggests that *B. subtilis* experiences higher drag force and is predicted to swim at a slower speed.

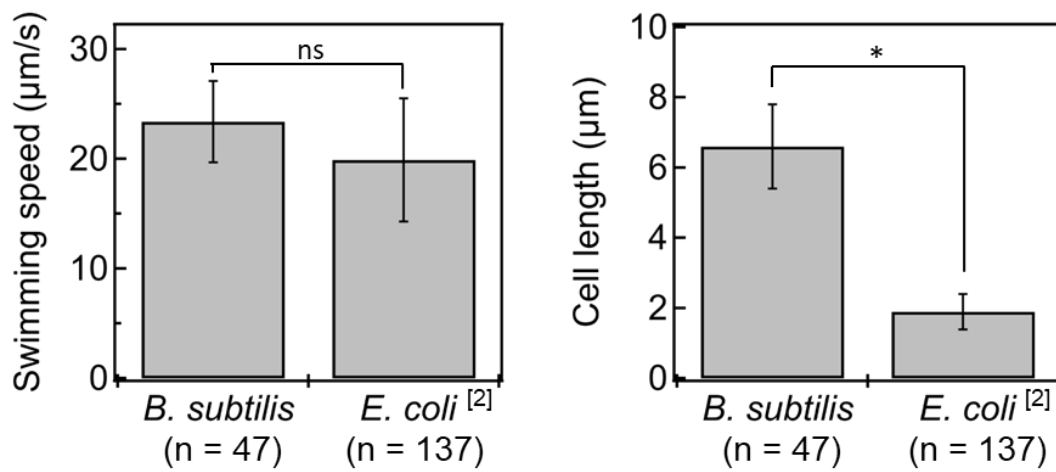


Figure IV-2. Swimming speed and cell length measurements.

Swimming bacteria were tracked and analyzed via custom-written Matlab code to determine the swimming speed and cell length. The *B. subtilis* results were compared to those of *E. coli* in literature [135]. The error bars indicate standard deviation.

Flagellar geometry

Next, we examined the role of flagellar filament geometry since it is one of the factors that determines the thrust force of the cell [136]. As previously described,

fluorescently labeled filaments were visualized. The images were analyzed using custom written Matlab code to determine the amplitude, pitch, and arc length (see Materials and Methods). Small differences in the three parameters were observed (Table IV-1).

Table IV-1. Flagellar geometry

	Amplitude, R (μm)	Pitch, λ (μm)	Arc length, L (μm)
<i>B. subtilis</i> (n=100)	0.3 ± 0.1	2.1 ± 0.3	7.3 ± 1.3
<i>E. coli</i> (n=50)	0.4 ± 0.1	2.7 ± 0.3	8.7 ± 2.0

Flagellar number

To quantify the number of flagellar filaments, we employed fluorescence visualization techniques. Strains with a cysteine mutation in the surface-exposed site of the flagellar protein were treated with maleimide-based fluorescent dye and visualized as described in Materials and Methods. Previously in our lab, we determined that *E. coli* has 3 ± 1 filaments per cell [137]. Normally, a 0.01% poly-L-lysine coated coverslip is employed to stick the cells and flagella down. However, the high number of flagella in *B. subtilis* resulted in filaments not sticking down, making it difficult to count. Therefore, a thin agar pad was placed on top of the cells to gently stick the filaments down. Despite these efforts, the number of filaments were still difficult to count. Thus, a straight filament mutant was employed, resulting in 8 ± 1 filaments per cell. The images of phase and fluorescently labeled flagella are shown in Figure IV-3.

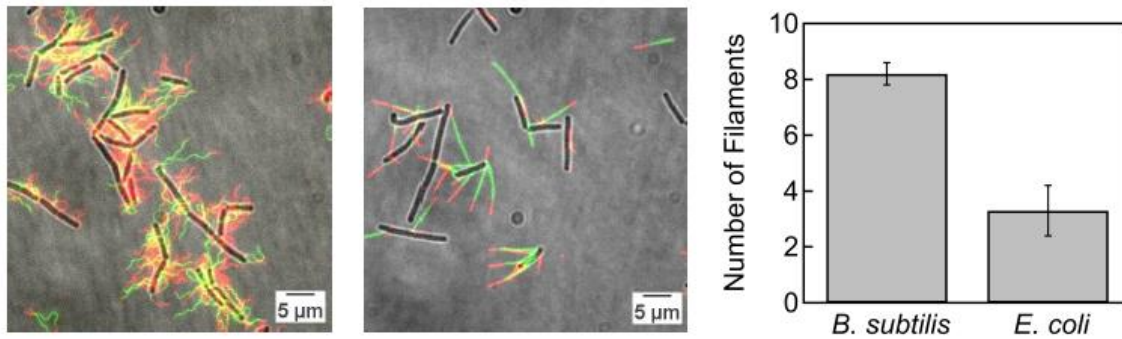


Figure IV-3. Fluorescently labeled filaments and their numbers.

Filaments of *B. subtilis* was labeled using fluorescent dyes. The green labeled filaments indicate filaments that grew until $OD_{600} \sim 0.5$ and red labeled filaments indicate filaments that grew for one hour after the green labeling. For wildtype (left), the flagellar filaments overlap with each other, making it difficult to count the exact number. This issue is resolved with the straight filament mutant (center). The bar graph compares the measured number of filaments in *B. subtilis* (n=25) to the reported value for *E. coli*. The error bars indicate standard deviation.

Although caution was taken to not shear the filaments while placing the agar pad, there were still concerns. To avoid this issue, we determined the number of hooks in both species by fluorescently labeling the hook protein with a cysteine mutation. Similar to the filament data, we observed that *B. subtilis* had twice as many hook foci compared to *E. coli* (Figure IV-4).

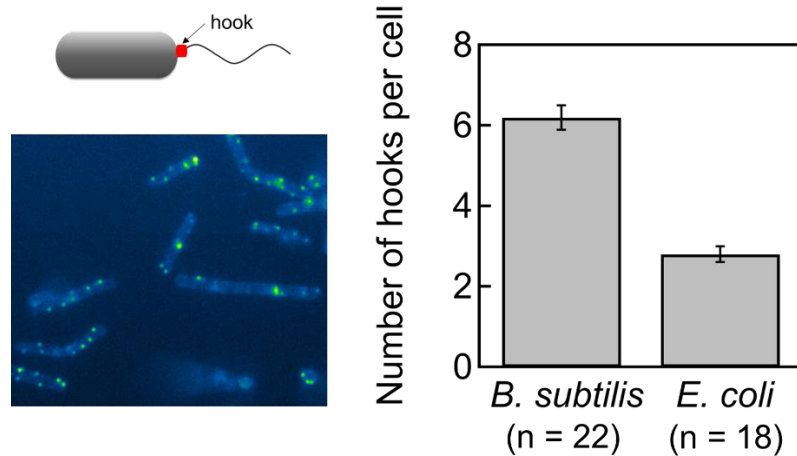


Figure IV-4. Fluorescently labeled hooks.

Flagellar hooks of *B. subtilis* (BD8207) and *E. coli* (PL237) were labeled fluorescently. The labeled hooks in *B. subtilis* is shown on the left. The bar graph (right) indicates the number of hooks counted per cell. The error bar indicate standard deviation.

Predicted rotational speed based on slender body theory

To relate the relationship between swimming speed and flagellar rotation speed, we used the propulsive matrix. Propulsive matrix performs force and torque balance to relate the translational and angular velocity with cell and flagellar geometry as constants [131]. One of the methods to solve the propulsive matrix is the slender body theory (SBT) [138, 139]. SBT agrees well with experimental swimming speeds of monotrichous species [140, 141]. Therefore, we used SBT to predict the flagellar rotational speed using the collected variables [141]. The predicted flagellar rotational speed ratio of *B. subtilis* to *E. coli* was 3.6, largely deviating from the experimental ratio of 0.7. The model predicted the rotational speed to be much higher in *B. subtilis* due to the longer cell length (higher drag force) and the similar swimming speed. The differences in the filament shapes did not compensate for the differences in the cell lengths. This model does not account for

differences in the flagellar numbers. However, previous theoretical works have suggested that the variations in filament numbers has negligible effect on the swimming speeds beyond 3 filaments; that is, whether a bug carries 3 or 8 filaments makes little difference to its swimming speed according to theory [142].

Direct comparison of swimming speed and membrane potential

We saw that a simple hydrodynamic analysis fails to recapitulate the swimming speed and flagellar rotation data in the two peritrichous species. This suggested that estimation of flagellar rotation speeds (and PMF) from swimming speeds is not an easy task. Hence, we directly compared the changes in the swimming speed and the membrane potential in the presence of a known protonophore, CCCP. We recorded videos of swimming *B. subtilis* in a dilute suspension of MB supplemented with various concentrations of CCCP. Cells were suspended in CCCP for 5 minutes to allow complete equilibrium before recording videos. The videos were analyzed to determine the percent changes in the swimming speed and the fraction of motile cells, as shown in Figure IV-5. Swimming speed in the absence of CCCP is used as a reference point to calculate the percent changes in the swimming speed. We observe a decrease in the swimming speed and the motile cell fraction as CCCP concentration increases. *B. subtilis* completely lost motility at 2 μM of CCCP.

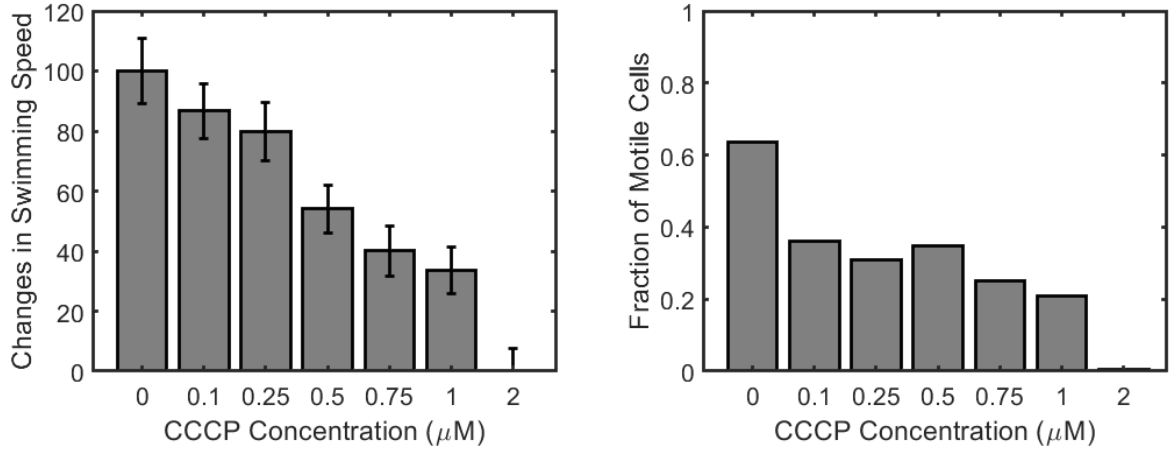


Figure IV-5. Swimming *B. subtilis* in the presence of CCCP.

Changes in the swimming speed are calculated with reference to cells in the absence of CCCP. Fraction of motile cells indicate the number of cells actively swimming compared to the total number of cells. The error bar indicates standard deviation.

Next, we measured the membrane potential over ranges of CCCP concentrations. The cells were treated with 10 μM Thioflavin T (ThT), a Nernstian dye, as the fluorescence signals from ThT are proportional to the membrane potential. A flow cell set-up was employed to measure the fluorescent signals changes with exposure to CCCP. Figure IV-6 is a representative graph of the fluorescent intensity over time for *B. subtilis* treated with 100 μM and 2 μM of CCCP. The pre-CCCP signal is collected over the first 60 seconds. Then, CCCP is introduced which leads to a decrease in the intensity. The data is collected for another 4 minutes for the signal to stabilize. The change in the intensity for pre- and post-stimulus is calculated to determine ΔI ($\Delta I = \frac{(I_{pre} - I_{post})}{I_{pre}}$). Cells exposed to 100 μM CCCP experience a complete loss of PMF and thus the change in signal is represented by $\Delta I_{control}$ [6] All other CCCP concentrations (0.1, 0.75, 2 μM) is represented by ΔI_{rest} . Using these values, we calculated the change in membrane potential

$(= \frac{(\Delta I_{control} - \Delta I_{test})}{\Delta I_{control}} * 100)$. We plotted the change in the swimming speed against the change in membrane potential for the corresponding CCCP concentrations as shown in Figure IV-7. The regime between 20-70% membrane potential is likely linear with respect to swimming speeds. However, more data points are needed. The fully characterized plot is expected to help estimate the PMF from swimming speeds.

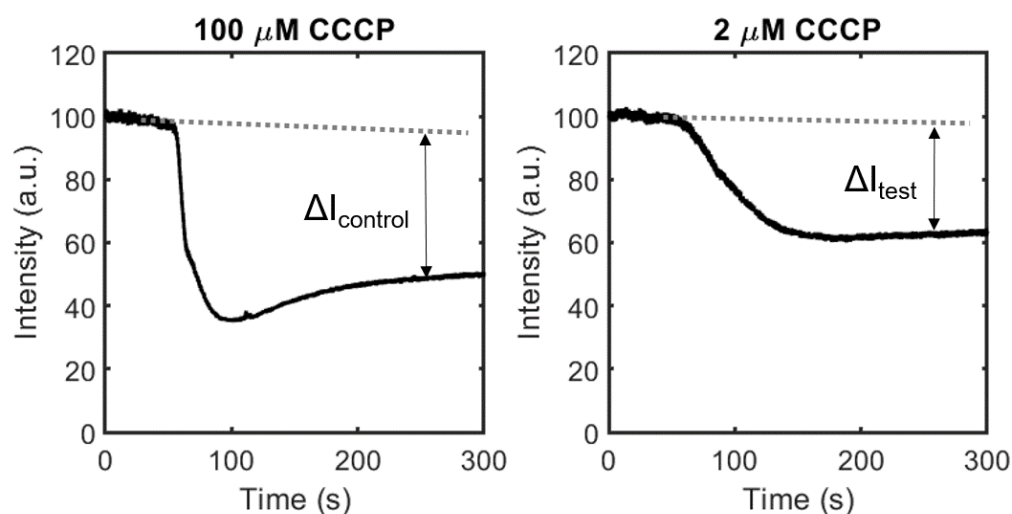


Figure IV-6. Fluorescence intensity of ThT over time.

Cells were suspended in 10 μM of ThT to quantify the membrane potential. The response of *B. subtilis* to 100 μM and 2 μM of CCCP is shown. The intensity decreases once it is exposed to CCCP. Here, we calculate the differences in the intensity for pre- and post-stimulus: $\Delta I_{control}$ and ΔI_{test} . We accommodate for dye photobleaching by extrapolating the pre-stimulus signal at the given time, as shown by the gray dotted line.

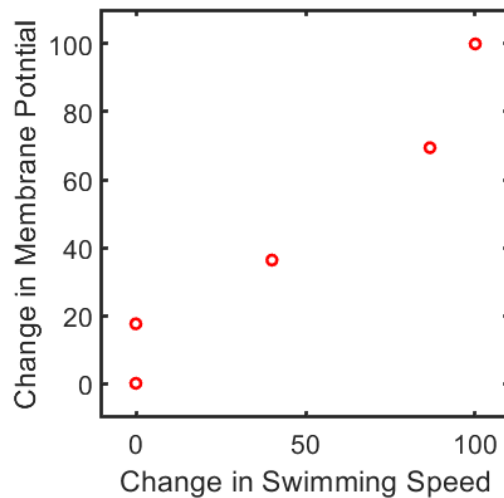


Figure IV-7. Change in swimming speed versus change in membrane potential.

The change in swimming speed and membrane potential was plotted for the following CCCP concentrations: 0, 0.1, 0.75, 2, and 100 μM . Here, we observe a linear region between the two variables.

Discussions

Here, we experimentally investigated the cell parameters of two peritrichous species to investigate whether swimming speed can be a PMF probe. We observed 30% lower flagellar rotation rate in *B subtilis* compared to that in *E. coli*. We hypothesized that we would observe a similar difference in the swimming speed as the swimming speed is proportional to the flagellar rotation rate, at least in monotrichous species. Surprisingly, the two peritrichous species swam at similar speeds. This may be because swimming speed is not solely a function of PMF but also many cell and flagellar parameters. We observed three times longer cell length, twice as many flagellar hooks, and significantly different flagellar geometry in *B. subtilis* compared to *E. coli*. Taking all but the flagellar numbers

in account with the aid of a hydrodynamic model, we predicted the flagellar rotational speed by solving the propulsive matrix with SBT. However, the predicted rotational speeds deviated from the experimental values. Therefore, we could not use hydrodynamic analysis to use swimming speed to accurately predict flagellar rotational speeds for peritrichous species.

One explanation for this discrepancy may be the difference in the number of flagella within the bundles that form in the two peritrichous species. However, theoretical studies suggest that the number of flagella do not affect swimming speeds much [142]. Our observations do suggest that the bundle diameter is two-fold higher in *B. subtilis* than in *E. coli* (Figure IV-8). We also observed multiple flagellar bundles on the same cell, consistent with previous observations [142, 143]. This could contribute to additional thrust forces, which may be compensating for the higher drag force and lower rotation rate in *B. subtilis*.

Our results indicated that there is not a predictable relationship between swimming speeds-flagellar rotation rates-PMF. Hence, we directly measured the swimming speed and membrane potential in *B. subtilis* while attenuating the PMF using CCCP. Preliminary data suggests a degree of linearity over a small regime in the membrane potential vs swimming speed data.

Supplementary Information

Table IV-2. Strain list

Strain	Information	Source
BD7816	IS75 hag T209C	[144]
BD7757	IS75 hag T209C A233V	[144]
BD8093	IS75 hagT209C motB::ery	[144]
BD8207	IS75 flgE T123C	[144]
BD8571	IS75 hag::tet amyE::Phag-hagsticky (hagT257I and fliCA386V) tet cat	David Dubnau lab
HCB1737	AW405 fliC_T254C	Howard Berg lab
PL237	RP437 Δ fliC Δ flgE pTrc99A-flgE_T124C	This work

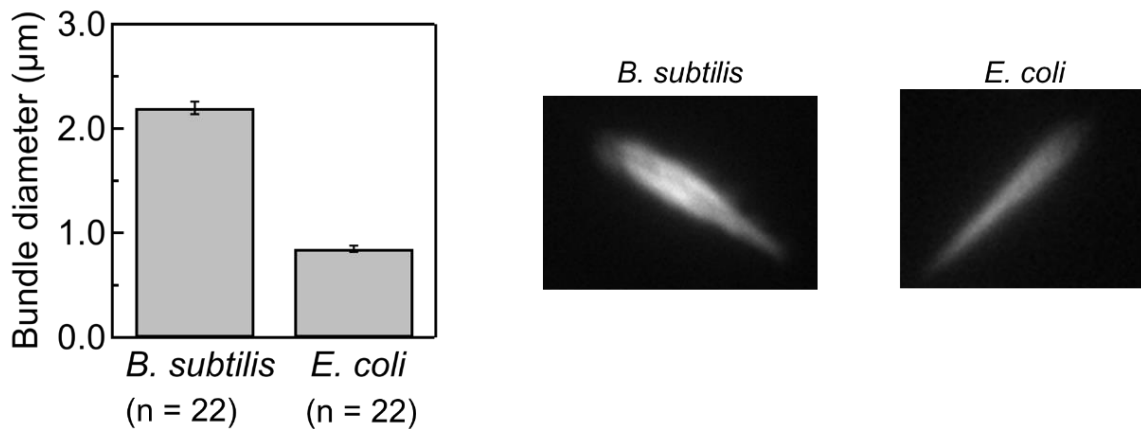


Figure IV-8. Bundle diameter measurement of swimming bacteria.

Videos of swimming cell with fluorescently labeled flagella were taken with 21 fps, as shown in the right. The error bars indicate standard errors.

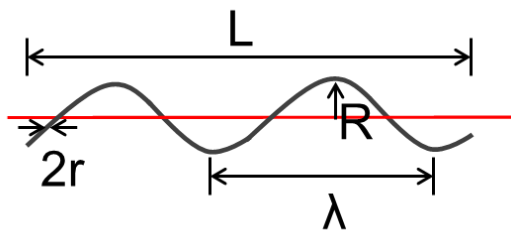


Figure IV-9. Polymorphic form of flagella.

The helical shape of flagella is depicted where L is the arc length, λ is the pitch, R is the amplitude and r is the helical radius.

CHAPTER V CHEMOTAXIS IN *CAULOBACTER CRESCENTUS*

Introduction

In the previous chapter, we saw how PMF influences swimming in peritrichous cells and the inaccuracies that arise inherently when attempting to predict swimming speeds from flagellar rotation rates with simple hydrodynamic models. This is largely because the assumptions of basic models are more appropriate for monotrichous, polarly-flagellated cells. As inter-filament hydrodynamic interactions and bundling complications do not exist in a monotrichous cell, such species are a better model system for our work. In this chapter, we worked with the model polar flagellate, *C. crescentus* [145]. As discussed in the introduction, very little is known about *C. crescentus*'s motility and chemotaxis. Hence, we shifted our focus to chemotaxis in this chapter.

Chemotaxis enables bacteria to navigate their surroundings as a response to chemical signals (see Background). For *C. crescentus*, several sugars and amino acids have been identified as attractants [68, 146]. But a major drawback is that agar plate assays incubated over several days were used to characterize chemotaxis. The spread of cells on the agar surface was considered to be a readout of chemotaxis [147, 148]. However, cell spreading in agar plate assays is dependent on multiple other confounding factors such as growth and metabolism. Furthermore, as these assays do not reveal single cell resolution, how cells chemotax remains unknown.

The peritrichous model species, *E. coli*, chemotax with run-tumble mechanism, as explained in the Background. Polar flagellates, in contrast, do not tumble but run and

reverse [64, 149, 150]. *C. crescentus* swims forward with CW rotation and backward with CCW rotation of its flagellum. In *E. coli*, the fraction of time that the flagellum rotates CW – CW_{bias} – indirectly reflects the changes in the chemotaxis kinase activity [151]. Attractants increase the CW_{bias} and repellents decrease it. However, in *C. crescentus*, the CW_{bias} is reportedly insensitive to attractants [62]. Instead, groups have suggested that monotrichous species including *C. crescentus* and *Pseudomonas aeruginosa*, modulate the frequency of reversals between forward and backward swimming in order to undergo chemotaxis [62-64]. Our lab has found that polarly-flagellated *Helicobacter pylori* modulates its CW_{bias} when stimulated with attractants [150]. It remains unclear whether polar flagellates undergo chemotaxis by only modulating reversal frequency or CW_{bias} or both.

Here, we measured single flagellar dynamics in *C. crescentus* over a range of xylose concentrations, as xylose is reported to be an attractant [68]. Analysis revealed that switching frequency increases above 150 μ M xylose while no significant changes were observed in CW_{bias} . To test how switching frequency affects chemotaxis at a population level, we employed a modified capillary assay. This revealed that there was a weak to no chemotaxis response towards the xylose within three minutes of observation. We also tested glucose, alanine, and galactose and observed a similar lack of chemotactic response. However, long time experiments with a transwell assay suggested weak chemotaxis over 15 minutes. We conclude that *C. crescentus* can undergo weak chemotaxis towards these stimulants, given adequate time. There was a weak but positive correlation between the switching frequency and attractant response to xylose. Our assay and approaches are

anticipated to reveal which compounds can induce a chemotactic response in *C. crescentus*.

Materials and Methods

Cell culturing

All *E. coli* experiments were done with the parent strain RP437. Overnight cultures were grown in Tryptone broth (TB) from isolated colonies. Day cultures were grown from overnight cultures in (1:100 dilution) in 10 mL fresh TB at 33°C. The cells were harvested at OD₆₀₀ ~ 0.4 - 0.6. For GFP expression in *E. coli*, plasmid pCM18 was used [152]. When needed, 100 µg/mL erythromycin was added to the cultures. All cells were washed in MB (0.01 M Phosphate buffer, 0.067 M NaCl, 10⁻⁴ M EDTA, 0.01 M Sodium Lactate, and 1 µM Methionine, pH ~ 7.0) before experiments.

All *C. crescentus* strains were derived from the parental strain NA1000. Overnight cultures were grown in peptone-yeast extract (PYE) from isolated colonies at 30°C. Day cultures were grown from overnight cultures in (1:100 dilution) in 10 mL fresh PYE at room temperature until cells were grown to early-exponential phase (OD₆₀₀ ~ 0.4 - 0.6). Strains lacking pili ($\Delta pila$) were grown in flasks and washed in MB before experiments. Wild-type cells were grown in petri dish to employ plate release method for cell life cycle synchronization [153]. For plate release method, the cells were gently rinsed with 10 mL of MB to remove all non-adherent cells. Then, 2 mL of PYE was added and left for 5 minutes to collect motile bacteria.

For GFP expression in *C. crescentus*, plasmid pXGFPC-2 with kanamycin resistance was used [154]. To maximize the GFP expression, the cells were grown in M2G (6.1 mM Na₂HPO₄, 3.9 mM KH₂PO₄, 9.3 mM NH₄Cl, 0.5 mM MgSO₄, 10 μM FeSO₄, 0.5 mM CaCl₂, 0.2% glucose) [155]. Additionally, 0.8 M xylose was administered to induce the GFP expression and kanamycin (5 μg/mL for liquid and 25 μg/mL for plates) was added.

Motor rotational measurements

Day cultures of $\Delta pilA$ strains were washed twice in MB via centrifugation (1500 × g for 5 min). Cells were resuspended in MB and aliquotted in small volumes in 1.5 mL centrifuge tubes. Cells were stimulated by adding appropriate concentration of xylose and pipetting. Cells were then loaded to glass slides and immediately imaged for one minute. Swimming cells spontaneously tethered to the glass surface due to surface hydrodynamics [156, 157]. Cell rotation was recorded on a Nikon microscope with a 40x objective with a dark field condenser at 60 fps and a digital camera (UI-3240LE-M-GL; IDS Imaging Development Systems). Videos of the rotation of tethered cells were analyzed with custom-written codes in MATLAB [156]. The rotation speeds were determined from Gaussian fits to the speed distributions. The CW_{bias} was calculated for each rotating cell for the duration of the video (< 1 minute). For the switching frequency, a switch in the direction was recognized if the cell made a full revolution or more.

Capillary assay

A Luer-stub (23 gauge, BD) fixed onto a 3-D custom printed holder was filled with ~0.5 mL of 1.5% molten agarose dissolved in MB, then soaked in 20 mL of indicated chemical overnight. The following day, cells were imaged in a culture-dish (Delta T system, Bioptechs Inc) with a Nikon Eclipse Ti-E equipped with a 10x or 20x phase objective. Cells from each experiment in MB were recorded for 30 seconds with a CCD camera (IDS model UI-3240LE) at 21 frames per second, pre-stimulus. Then, the prepared Luer-stub was introduced to the T-dish as close to the glass surface, and post-stimulus video was recorded for three minutes. The video was analyzed using a custom-written particle tracking Matlab code to track the number of cells in the field of view.

Transwell assay

The transwell assay was conducted as described previously [158]. Transwell inserts with a 0.4 μm pore size membrane filter was used for this experiment (ThermoFisher). Outside of the membrane filter was coated with 0.01% poly-L-lysine. Then, molten agarose (1.5% w/v) was poured inside the insert and soaked overnight in MB or 100 mM of the chemo-effector. The next day, a dilute suspension of GFP-expressing cells was washed in MB and added to the well plate. After 5 minutes, the transwell insert was transferred to the well-plate to make contact with the cell suspension. After 15 minutes, the inserts were removed and washed gently in MB. Then, the inserts are left to dry in an inverted position. Cell attachment was imaged using a confocal microscope with a 10x objective and analyzed using a custom written Matlab code.

Results

Single cell flagellar dynamics

A popular method to measure the chemotactic response of single cells is using tethered-cell assay to track the CW_{bias} . Often, perfusion chambers are employed to stimulate the cells with chemo-effectors [158]. However, this method requires a sticky flagellar mutant, which has not been isolated in *C. crescentus*. Hence, we opted to a different approach to characterize the CW_{bias} in *C. crescentus*. In earlier works, single swimming cells lacking pili spontaneously adhere to the glass surface via a fluid joint and rotate similar to tethered cells due to the hydrodynamic interactions of the flagellum and the surface [156]. Due to this coupling, when the flagellum rotates CW, the cell body rotates CCW and vice versa. To study the transient response of the CW_{bias} to step changes in the chemo-effector concentrations, we would mix the chemo-effector and the cells in a vial by pipetting and immediately introduce the suspension for observation under the microscope. Between mixing and the time of observation, we would usually lose no more than 10 seconds of the response. Introduction of the suspension in the tunnel slide would immediately result in transient coupling of several cells to the surface. These couplings lasted for a minute typically before the cells escaped back into the suspension. This minute of observation was adequate for recording the post-stimulus CW_{bias} using phase contrast microscopy. Figure V-1 depicts how videos of rotating cells can be tracked through Matlab to obtain a circular trajectory. Videos of rotating cells were analyzed to calculate the CW_{bias} , switching frequency, and the rotational speed (Figure V-2).

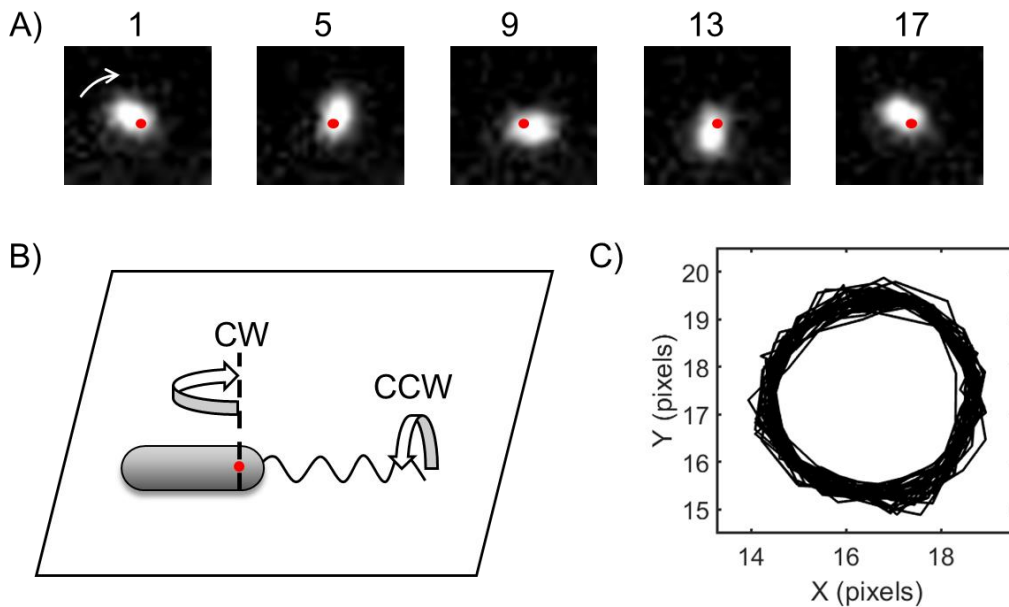


Figure V-1. Schematic of transiently tethered cells.

A) A video of transiently tethered cells were recorded. The cell rotates in a CCW direction at the center of rotation (red circle). The numbers at the top of each image indicates the frame of the video. B) A schematic of how CCW rotation of the flagellum induces a CW rotation of the cell body. C) The trajectory of the rotating cell in (A) analyzed using Matlab.

We employed this method to compare the pre- and post-stimulus CW_{bias} over a range of xylose concentrations (15 μM to 15 mM). Interestingly, the pre-stimulus CW_{bias} was approximately 0.5 compared to the reported 0.8 [156]. Upon introduction of xylose, the CW_{bias} increased slightly. Additionally, the switching frequency increased by approximately two-fold. Both positive and negative rotational speed decreased slightly but not significantly with xylose concentration.

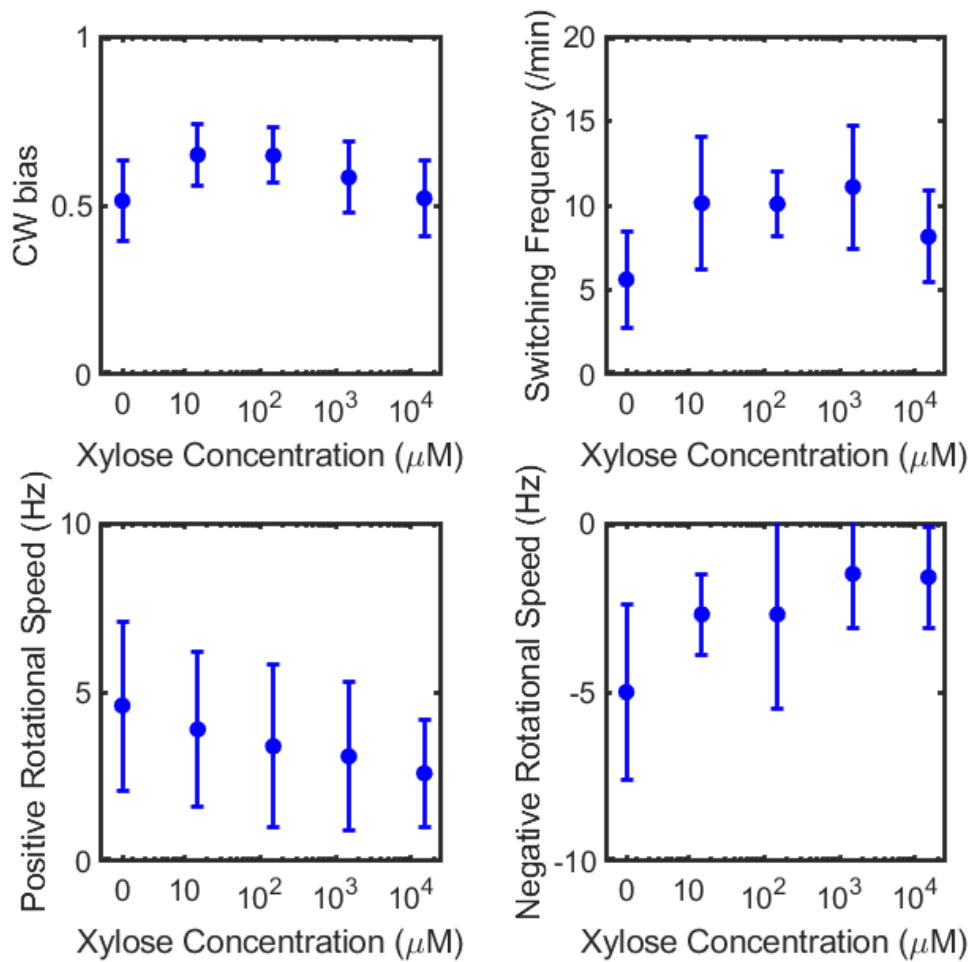


Figure V-2. Flagellar motor dynamic changes with xylose concentration.

The CW_{bias} (top left), switching frequency (top right), and rotational speed (bottom) for IPL1 was measured for various concentrations: 0 μM (n=15), 15 μM (n=18), 150 μM (n=26), 1.5 mM (n=16), and 15 mM (n=15). The error bars indicate standard errors. With xylose, there is a slight increase in the CW_{bias} and the switching frequency increases up to two-fold. The positive and negative rotational speed decreases gradually with increasing xylose concentration.

Micro-capillary assay

To assess whether changes in the flagellar dynamics promote chemotaxis, we used a modified capillary assay to expose a population of swimming cells to a point source of

chemo-effector, as shown in Figure V-3. A Luer stub was filled with molten agarose that was soaked overnight in MB or 100 mM of chemo-effector. The next day, an open petri dish was filled with 1.3 mL of cells suspended in MB. Then, we recorded the swimming cells as a measure of the pre-stimulus behavior and introduced the Luer stub filled with chemo-effector into the pool of swimming bacteria using a micromanipulator. The cell response to this point source in the field of view was then recorded for the next three minutes.

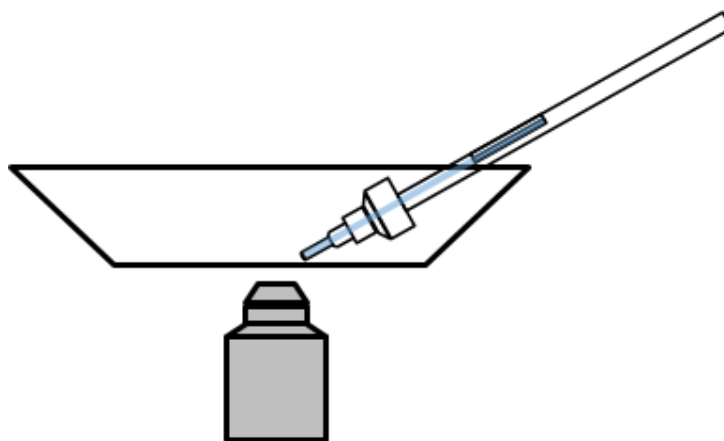


Figure V-3. Schematic of the modified capillary assay

The 3D printed Luer stub holder with a cavity is filled with molten agarose that has been soaked overnight in MB or 100 mM of chemo-effector. Before the experiment, the Luer stub is positioned as close to the surface of the glass petri dish. Then, during pre-stimulus measurements, the Luer stub is raised up. During post-stimulus, the Luer stub is immediately brought down to record the response of the cells.

As a positive control for our experimental setup, we first performed experiments with *E. coli* and a known *E. coli* attractant, serine [159]. Videos of swimming cells in the absence and presence of serine were recorded and analyzed by particle tracking algorithm to count the changes in the number of cells in the field of view before and after stimulus.

Before cells were exposed to the point source (pre-stimulus), the number of cells in the field of view remained fairly constant (Figure V-4, top). Post-stimulus, the number of cells rapidly increased for 100mM serine, showing a strong attractant response. When the fluid in the Luer stub was replaced with MB, there was no change in the number of cells.

We tested the response of *C. crescentus* to four different compounds reported as attractants [68]: xylose, glucose, alanine, and galactose. Bottom of Figure V-4 shows the number of *C. crescentus* cells in the field of view for pre and post-stimulus. We did not observe the strong response seen for *E. coli*. Instead, the post-stimulus response was comparable with the MB. To analyze the post-stimulus response further, we plotted the relative changes in the number of cells against the data for MB (Figure V-5). We observed a weak attractant response from xylose and glucose and a weak repellent response from alanine and galactose.

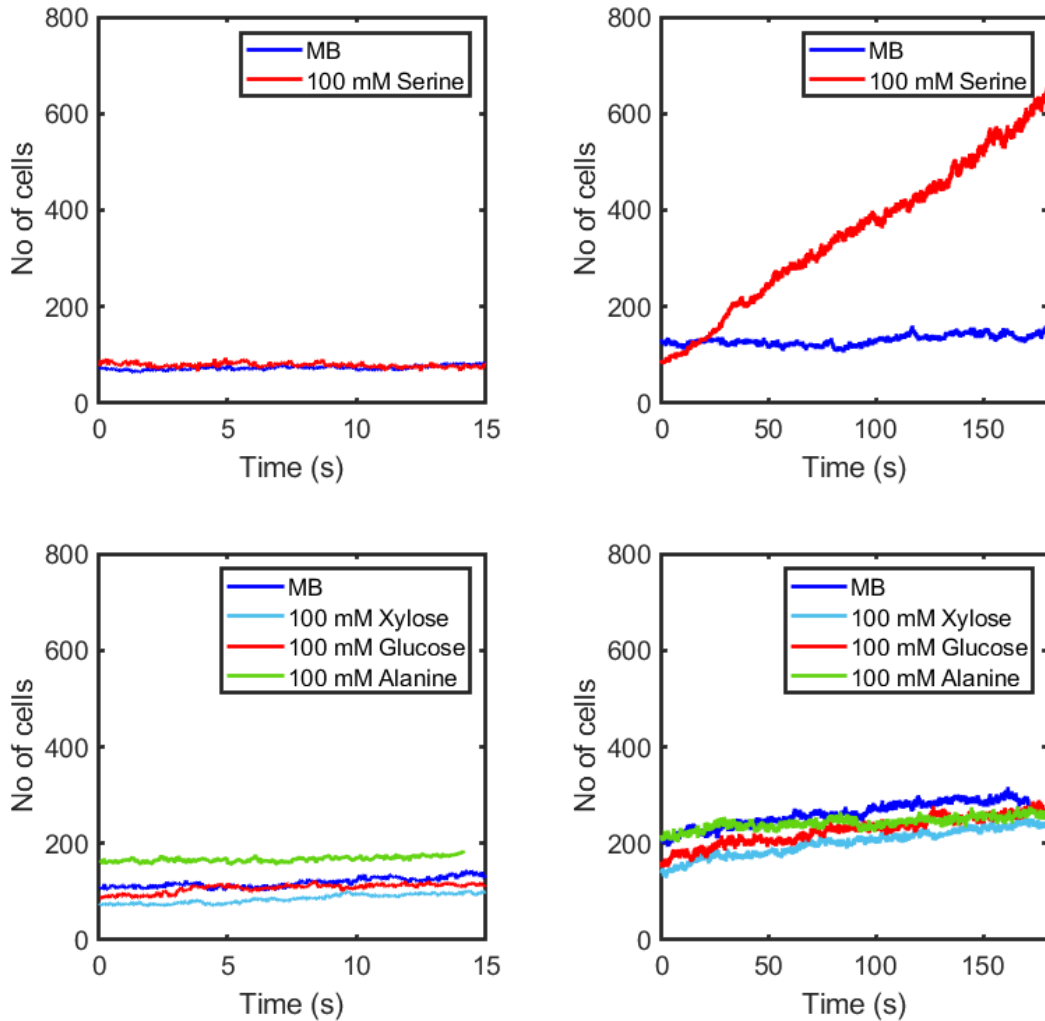


Figure V-4. Number of cells with exposure to a point source.

The number of cells that attract in the field of view over time are plotted for for *E. coli* (top) and *C. crescentus* (bottom). The pre-stimulus (left) and post-stimulus (right) indicates before and after Luer stub is inserted into the medium, respectively. The pre-stimulus values for all species is fairly constant. For *E. coli*, there is a steep increase for serine compared to MB, indicating attractant response for serine. However, the xylose, glucose, and alanine behave similarly to MB for *C. crescentus*, which does not seem to attract towards the Luer stub.

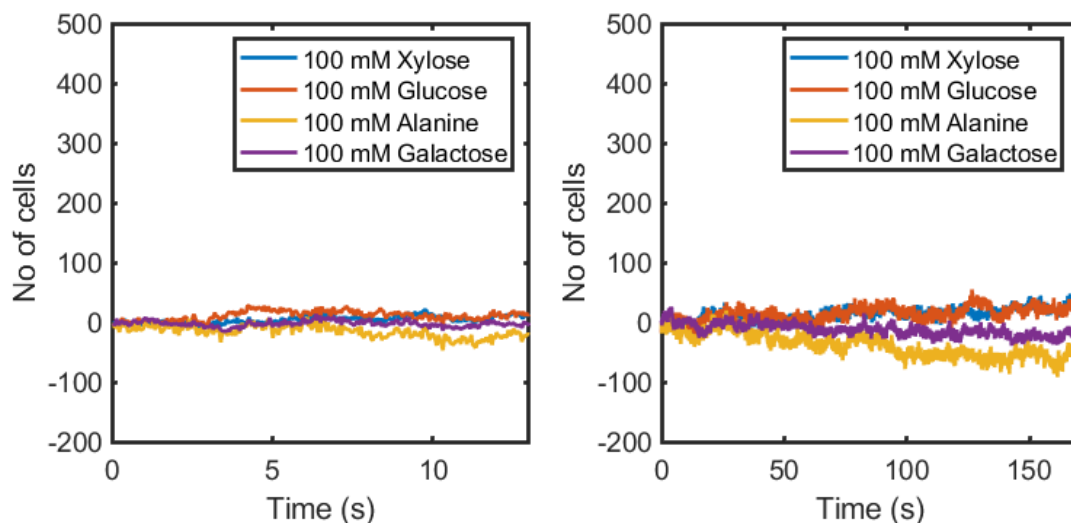


Figure V-5. Relative number of cells with exposure to a point source.

The relative number of cells were calculated by scaling to the number of cells observed for MB. The pre-stimulus (left) value remains approximately at zero for all chemo-effectors (100 mM xylose, glucose, alanine, and galactose). For the post-stimulus (right), some deviation from the zero value is shown. With xylose and glucose, there is a weak attractant response (relative number of cells < 50). With alanine and galactose, there is a weak repellent response (relative number of cells > -50).

Transwell assay to test longer dynamics

We measured the chemotaxis response over short periods of time using the single cell tethered assays and Luer stub capillary assay (1 to 3 minutes). Previously, chemotaxis for *C. crescentus* was observed using agar plate assay over 3 to 5 days [147, 148]. Traditionally, 15 to 30 minutes is enough to observe migration in *E. coli* [57]. Therefore, we conducted transwell assay, previously developed, to observe migration of cells over 15 minutes [158, 160, 161]. Soaked agar pads containing MB or 100 mM chemo-effector was brought in contact with a pool of swimming cells in MB. Upon contact with the agar

pads, a chemo-effector gradient was established. Cells responded by either swimming towards (attractant) or away (repellent) from the agar surface. When cells swam towards the surface, they became irreversibly attached due to poly-L-lysine coating. After 15 minutes of exposure, the number of attached cells were counted. The chemo-effector was serine and xylose for *E. coli* and *C. crescentus*, respectively. As shown in Figure 3, *E. coli* cells that were exposed to the agar pads containing 100 mM serine attached by a number 4-fold greater than cells exposed to agar pads containing MB, indicating a strong attractant response. For *C. crescentus*, there was a 2-fold greater attachment in 100 mM xylose. Interestingly, this may suggest that the attractant response for *C. crescentus* is dependent on time.

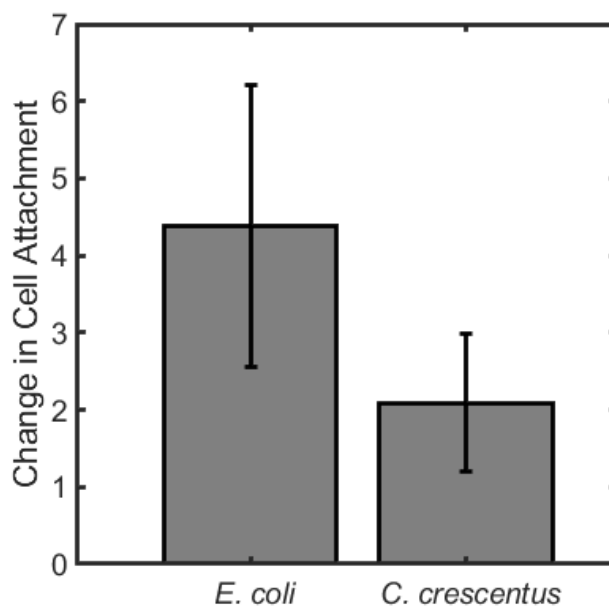


Figure V-6. The observed chemotaxis response using transwell assay.

The change in cell attachment is calculated by the fold-change in number of attached cells in 100 mM chemo-effector (serine for *E. coli* and xylose for *C. crescentus*) compared to

that in MB. An attractant response is observed for both species. The error bar is determined from three biological and four technical replicates.

Discussions

Polar flagellates are predicted to modulate reversal frequencies rather than the CW_{bias} to chemotax. This is because CW_{bias} modulation increases the chance of errors, making it difficult for bacteria to reach the destination. Previous work with *C. crescentus* diffused chemo-effectors through agar plate assays to test for chemotaxis. However, these assays need to be incubated for 3 to 5 days, preventing any possibility of measuring flagellar behavior during chemotaxis. Microfluidic chambers have also been developed to visualize the swimming behavior of each cell in chemical fields. However, these are not as powerful as the single motor assays that we have used in this work.

Our single motor assays rely on hydrodynamic coupling of the filament and the surface [156]. We used the approach to study the response to chemo-effectors. We observed motor behavior over one minute. Reversal frequency and CW_{bias} increased at single cell level in the presence of chemoeffectors. This is a promising technique except that the trajectories are short-lived – cells can transiently detach and swim away from the surface during the experiment. Also, we always missed the first 10 seconds of data as it took time to introduce the cells from the vial into the tunnel slide and to focus the microscope. We may be missing some adaptative behavior before the cells are imaged.

Despite the limitations of our method, we observed a weak increase in the CW_{bias} when cells were exposed to xylose, consistent with predictions from other works. The reversal frequency increased by two-fold even at 15 μM of xylose. Surprisingly,

chemotaxis was poor in *C. crescentus*. Over long times, some chemotaxis was seen and a weak, but positive correlation existed between reversal frequency and chemotaxis. Given the numerous CheY-like regulators, such weak chemotaxis indicates alternate roles for the chemotaxis network. However, more experiments are needed with other chemoeffectors to rigorously test this idea.

Supplementary Information

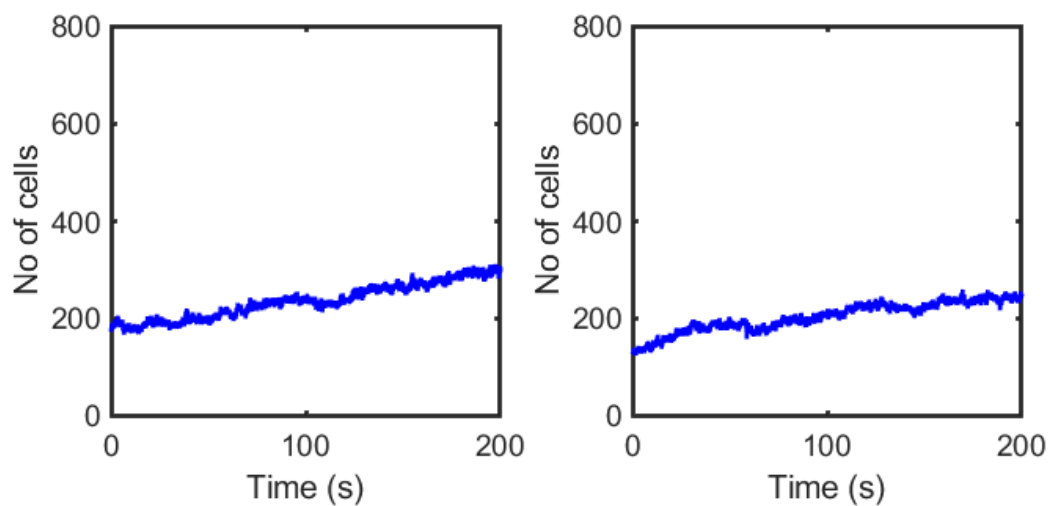


Figure V-7. Basal level in the number of cells over time for *C. crescentus* strains. Within 200 seconds, the number of cells increased 1.7 and 1.9 times for $\Delta pilA$ (left) and wildtype (right), respectively. Therefore, $\Delta pilA$ strain is more suitable to use for further Luer stub capillary assays.

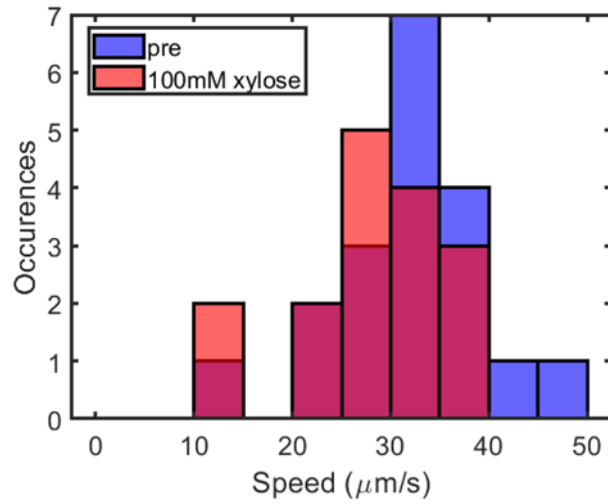


Figure V-8. Swimming speed of *C. crescentus*.

The swimming speed of IPL1 ($\Delta pilA$) was measured during the Luer stub capillary assay. A histogram is plotted for the speeds measured at pre-stimulus and post-stimulus with 100 mM xylose. The swimming speed decreased from $32.6 \pm 7.6 \mu\text{m/s}$ (pre-stimulus) to $28.7 \pm 8.0 \mu\text{m/s}$ (post-stimulus).

CHAPTER VI CONCLUSIONS AND FUTURE WORK

PMF is an exciting feature to study because of its important role in cell physiology. As one of the key energy sources that powers bacterial processes, it is crucial to quantify the PMF. PMF is known to drive bacterial motility through flagellar rotation. Thus, we focused on investigating the effect of PMF in bacterial motility and chemotaxis.

In Chapter 3, we developed an analytical model which extended the application of intensity-based GFP as a probe of intracellular pH. We first experimentally quantifying the pH-sensitive response of both intensity-based and ratiometric fluorescent proteins expressed in Gram-negative *E. coli*. Then, an analytical model that incorporated the emission intensity from the two states of the chromophore was developed. A key finding from the analytical model is that the scaling analysis eliminated the dependence of protein concentration for GFP. Our analysis revealed that ratiometric are error-prone as their emission ratios depend on equipment, which varies from one lab to another. Our work paves the way for researchers to use the more convenient intensity-based proteins instead of ratiometric proteins as a pH probe.

In Chapter 4, we investigated the use of swimming motility as a PMF probe for peritrichous bacteria, *E. coli* and *B. subtilis*. As flagellar rotation speed is not straight forward in all species, we delved into the quantitative relationship between swimming speeds and the flagellar rotation speed in *B. subtilis*. We experimentally determined various cell and flagellar properties for both species. The values for these parameters were used to predict the flagellar rotation speeds. However, there was a large discrepancy

between the experimental and predicted values. We suggest that the discrepancy arises from flagellar interactions with one another in peritrichous species. To probe this further, an intensive hydrodynamic analysis should be conducted in the future.

To circumvent hydrodynamic complications, we directly measured the relationship between swimming speed and membrane potential in *B. subtilis* and observed linearity over a small regime. Measurements of swimming speeds can reveal changes in the PMF in this regime for *B. subtilis*. In the future, we hope to obtain more data points to fully characterize the quantitative relationship between PMF and swimming speed in this and other species.

In Chapter 5, we investigated the response of *C. crescentus* for various chemo-effectors. To determine the mechanism behind chemotaxis in polar-flagellated *C. crescentus*, we observed transiently-tethered cells. A mild increase in the CW_{bias} and the reversal frequency was observed upon xylose. To understand how the changes in the flagellar dynamics affect the performance of chemotaxis, we developed a modified capillary assay using Luer stub. Here, we saw weak to no migration towards the xylose point source. Interestingly, upon longer time incubation with xylose, a weak attractant response was recorded. This work tested a link between the flagellar dynamics and chemotaxis performance in *C. crescentus*, and found a weak correlation. Future work could focus on testing response to other chemo-effectors. If a strong chemo-effector is found, the role of CheY homologs in *C. crescentus* could be determined as they are suggested to compete with the CheYII, which behaves similarly to the CheY in *E. coli*. These CheY homologs are capable of interacting with the motor and induce changes in

the swimming speed and the motor switches. It could be that the weak attractant response with xylose is due to the competition of CheYs. But then the purpose of the chemotaxis network is unclear in *C. crescentus*. The weak chemotactic responses is even more unexpected considering that *C. crescentus* has an abundant number of chemoreceptors compared to *E. coli*. Therefore, future work should focus on the precise functions of these proteins.

REFERENCES

1. Mitchell, P., *Coupling of Phosphorylation to Electron and Hydrogen Transfer by a Chemi-Osmotic type of Mechanism*. Nature, 1961. **191**(4784): p. 144-148.
2. Maloney, P.C., E.R. Kashket, and T.H. Wilson, *A Protonmotive Force Drives ATP Synthesis in Bacteria*. 1974. **71**(10): p. 3896-3900.
3. Damper, P.D. and W. Epstein, *Role of the membrane potential in bacterial resistance to aminoglycoside antibiotics*. 1981. **20**(6): p. 803-808.
4. Goode, O., et al., *Persister Escherichia coli Cells Have a Lower Intracellular pH than Susceptible Cells but Maintain Their pH in Response to Antibiotic Treatment*. **0**(0): p. e00909-21.
5. Krulwich, T.A., G. Sachs, and E. Padan, *Molecular aspects of bacterial pH sensing and homeostasis*. Nature reviews. Microbiology, 2011. **9**(5): p. 330-343.
6. Strahl, H. and L.W. Hamoen, *Membrane potential is important for bacterial cell division*. 2010. **107**(27): p. 12281-12286.
7. Prindle, A., et al., *Ion channels enable electrical communication in bacterial communities*. Nature, 2015. **527**(7576): p. 59-63.
8. Humphries, J., et al., *Species-Independent Attraction to Biofilms through Electrical Signaling*. Cell, 2017. **168**(1): p. 200-209.e12.
9. Poole, R.J., *Energy Coupling for Membrane Transport*. 1978. **29**(1): p. 437-460.
10. Manson, M.D., et al., *A protonmotive force drives bacterial flagella*. 1977. **74**(7): p. 3060-3064.

11. Gabel, C.V. and H.C. Berg, *The speed of the flagellar rotary motor of Escherichia coli varies linearly with protonmotive force*. Proc Natl Acad Sci U S A, 2003. **100**(15): p. 8748-51.
12. Kikuchi, K., et al., *The application of the Escherichia coli giant spheroplast for drug screening with automated planar patch clamp system*. Biotechnology reports (Amsterdam, Netherlands), 2015. **7**: p. 17-23.
13. Martinac, B., et al., *Pressure-sensitive ion channel in Escherichia coli*. 1987. **84**(8): p. 2297-2301.
14. Nakamura, K., et al., *Patch clamp analysis of the respiratory chain in Bacillus subtilis*. Biochimica et Biophysica Acta (BBA) - Biomembranes, 2011. **1808**(4): p. 1103-1107.
15. Sirec, T., et al., *Electrical Polarization Enables Integrative Quality Control during Bacterial Differentiation into Spores*. iScience, 2019. **16**: p. 378-389.
16. Matsuyama, T., *Staining of living bacteria with rhodamine 123*. FEMS Microbiology Letters, 1984. **21**(2): p. 153-157.
17. Resnick, M., S. Schuldiner, and H. Bercovier, *Bacterial membrane potential analyzed by spectrofluorocytometry*. Current Microbiology, 1985. **12**(4): p. 183-185.
18. López-Amorós, R., et al., *Assessment of E. coli and Salmonella viability and starvation by confocal laser microscopy and flow cytometry using rhodamine 123, DiBAC4(3), propidium iodide, and CTC*. 1997. **29**(4): p. 298-305.

19. Hudson, M.A., D.A. Siegele, and S.W. Lockless, *Use of a Fluorescence-Based Assay To Measure Escherichia coli Membrane Potential Changes in High Throughput*. 2020. **64**(9): p. e00910-20.
20. Novo, D., et al., *Accurate flow cytometric membrane potential measurement in bacteria using diethyloxycarbocyanine and a ratiometric technique*. 1999. **35**(1): p. 55-63.
21. Stratford, J.P., et al., *Electrically induced bacterial membrane-potential dynamics correspond to cellular proliferation capacity*. 2019. **116**(19): p. 9552-9557.
22. Mancini, L., et al., *A General Workflow for Characterization of Nernstian Dyes and Their Effects on Bacterial Physiology*. *Biophysical Journal*, 2020. **118**(1): p. 4-14.
23. Chaloupka, R., et al., *Measurement of membrane potential in Saccharomyces cerevisiae by the electrochromic probe di-4-ANEPPS: effect of intracellular probe distribution*. *Folia Microbiol (Praha)*, 1997. **42**(5): p. 451-6.
24. Suchodolski, J. and A. Krasowska, *Plasma Membrane Potential of Candida albicans Measured by Di-4-ANEPPS Fluorescence Depends on Growth Phase and Regulatory Factors*. *Microorganisms*, 2019. **7**(4): p. 110.
25. Kralj, J.M., et al., *Electrical Spiking in Escherichia coli Probed with a Fluorescent Voltage-Indicating Protein*. 2011. **333**(6040): p. 345-348.
26. Nadeau, J., *Initial photophysical characterization of the proteorhodopsin optical proton sensor (PROPS)*. 2015. **9**.

27. Zajdel, T.J., et al. *Probing the dynamics of the proton-motive force in E. coli.* in *SENSORS, 2014 IEEE.* 2014.
28. Felle, H., et al., *Quantitative measurements of membrane potential in Escherichia coli.* *Biochemistry*, 1980. **19**(15): p. 3585-3590.
29. Letellier, L. and E. Shechter, *Cyanine dye as monitor of membrane potentials in Escherichia coli cells and membrane vesicles.* *Eur J Biochem*, 1979. **102**(2): p. 441-7.
30. Zilberstein, D., et al., *The sodium/proton antiporter is part of the pH homeostasis mechanism in Escherichia coli.* *Journal of Biological Chemistry*, 1982. **257**(7): p. 3687-3691.
31. Slonczewski, J.L., et al., *pH homeostasis in Escherichia coli: measurement by ³¹P nuclear magnetic resonance of methylphosphonate and phosphate.* *Proc Natl Acad Sci U S A*, 1981. **78**(10): p. 6271-6275.
32. Miesenbock, G., D.A. De Angelis, and J.E. Rothman, *Visualizing secretion and synaptic transmission with pH-sensitive green fluorescent proteins.* *Nature*, 1998. **394**(6689): p. 192-5.
33. Ingledew, W. and R.J.A. Kroll, *Microbiology of extreme environments.* 1990, McGraw-Hill: New York.
34. Berg, H.C. and R.A. Anderson, *Bacteria Swim by Rotating their Flagellar Filaments.* *Nature*, 1973. **245**(5425): p. 380-382.
35. Reid, S.W., et al., *The maximum number of torque-generating units in the flagellar motor of Escherichia coli is at least 11.* 2006. **103**(21): p. 8066-8071.

36. Pourjaberi, S.N.S., et al., *The role of a cytoplasmic loop of MotA in load-dependent assembly and disassembly dynamics of the MotA/B stator complex in the bacterial flagellar motor*. Mol Microbiol, 2017. **106**(4): p. 646-658.
37. Berg, H.C., *Bacterial flagellar motor*. Current Biology, 2008. **18**(16): p. R689-R691.
38. Biquet-Bisquert, A., et al., *The Dynamic Ion Motive Force Powering the Bacterial Flagellar Motor*. 2021. **12**.
39. Silverman, M. and M. Simon, *Flagellar rotation and the mechanism of bacterial motility*. Nature, 1974. **249**(452): p. 73-4.
40. Kuwajima, G., *Flagellin domain that affects H antigenicity of Escherichia coli K-12*. Journal of bacteriology, 1988. **170**(1): p. 485-488.
41. Kuwajima, G., *Construction of a minimum-size functional flagellin of Escherichia coli*. Journal of bacteriology, 1988. **170**(7): p. 3305-3309.
42. Chen, X. and H.C. Berg, *Torque-speed relationship of the flagellar rotary motor of Escherichia coli*. Biophys J, 2000. **78**(2): p. 1036-41.
43. Lele, P.P., B.G. Hosu, and H.C. Berg, *Dynamics of mechanosensing in the bacterial flagellar motor*. 2013. **110**(29): p. 11839-11844.
44. Scharf, B.E., et al., *Control of direction of flagellar rotation in bacterial chemotaxis*. 1998. **95**(1): p. 201-206.
45. Fung, D.C. and H.C. Berg, *Powering the flagellar motor of Escherichia coli with an external voltage source*. Nature, 1995. **375**(6534): p. 809-812.

46. Manson, M.D., P.M. Tedesco, and H.C. Berg, *Energetics of flagellar rotation in bacteria*. Journal of Molecular Biology, 1980. **138**(3): p. 541-561.
47. Khan, S., M. Meister, and H.C. Berg, *Constraints on flagellar rotation*. Journal of Molecular Biology, 1985. **184**(4): p. 645-656.
48. Khan, S., M. Dapice, and I. Humayun, *Energy transduction in the bacterial flagellar motor. Effects of load and pH*. Biophys J, 1990. **57**(4): p. 779-96.
49. Lo, C.-J., et al., *Nonequivalence of Membrane Voltage and Ion-Gradient as Driving Forces for the Bacterial Flagellar Motor at Low Load*. Biophysical Journal, 2007. **93**(1): p. 294-302.
50. Terahara, N., et al., *Load- and polysaccharide-dependent activation of the Na⁺-type MotPS stator in the Bacillus subtilis flagellar motor*. Scientific Reports, 2017. **7**(1): p. 46081.
51. Terahara, N., et al., *Na⁺-induced structural transition of MotPS for stator assembly of the Bacillus flagellar motor*. 2017. **3**(11): p. eaao4119.
52. Ito, M., et al., *Properties of motility in Bacillus subtilis powered by the H⁺-coupled MotAB flagellar stator, Na⁺-coupled MotPS or hybrid stators MotAS or MotPB*. J Mol Biol, 2005. **352**(2): p. 396-408.
53. Ito, M., et al., *Properties of motility in Bacillus subtilis powered by the H⁺-coupled MotAB flagellar stator, Na⁺-coupled MotPS or hybrid stators MotAS or MotPB*. 2005. **352**(2): p. 396-408.

54. Terahara, N., et al., *An Intergenic Stem-Loop Mutation in the <i>Bacillus subtilis ccpA-motPS</i> Operon Increases <i>motPS</i> Transcription and the MotPS Contribution to Motility*. 2006. **188**(7): p. 2701-2705.
55. Ito, M., et al., *Properties of Motility in Bacillus subtilis Powered by the H⁺-coupled MotAB Flagellar Stator, Na⁺-coupled MotPS or Hybrid Stators MotAS or MotPB*. Journal of Molecular Biology, 2005. **352**(2): p. 396-408.
56. Darnton, N.C., et al., *On Torque and Tumbling in Swimming <i>Escherichia coli</i>*. 2007. **189**(5): p. 1756-1764.
57. Adler, J.J.M., *A method for measuring chemotaxis and use of the method to determine optimum conditions for chemotaxis by Escherichia coli*. 1973. **74**(1): p. 77-91.
58. Macnab, R.M., *Bacterial flagella rotating in bundles: a study in helical geometry*. Proc Natl Acad Sci U S A, 1977. **74**(1): p. 221-5.
59. Berg, H.C., *E. coli in Motion*. 2008: Springer Science & Business Media.
60. Larsen, S.H., et al., *Change in direction of flagellar rotation is the basis of the chemotactic response in Escherichia coli*. Nature, 1974. **249**(452): p. 74-7.
61. Sourjik, V. and N.S. Wingreen, *Responding to chemical gradients: bacterial chemotaxis*. Current opinion in cell biology, 2012. **24**(2): p. 262-268.
62. Grognot, M. and K.M. Taute, *A multiscale 3D chemotaxis assay reveals bacterial navigation mechanisms*. Communications Biology, 2021. **4**(1): p. 669.
63. Kovarik, M.L., et al., *Microchannel-Nanopore Device for Bacterial Chemotaxis Assays*. Analytical Chemistry, 2010. **82**(22): p. 9357-9364.

64. Cai, Q., et al., *Singly Flagellated Pseudomonas aeruginosa Chemotaxes Efficiently by Unbiased Motor Regulation*. 2016. **7**(2): p. e00013-16.
65. Alley, M.R., et al., *Genetic analysis of a temporally transcribed chemotaxis gene cluster in Caulobacter crescentus*. *Genetics*, 1991. **129**(2): p. 333-41.
66. Alley, M.R., J.R. Maddock, and L. Shapiro, *Polar localization of a bacterial chemoreceptor*. *Genes Dev*, 1992. **6**(5): p. 825-36.
67. Alley, M.R., J.R. Maddock, and L. Shapiro, *Requirement of the carboxyl terminus of a bacterial chemoreceptor for its targeted proteolysis*. *Science*, 1993. **259**(5102): p. 1754-7.
68. Ely, B., et al., *General nonchemotactic mutants of Caulobacter crescentus*. *Genetics*, 1986. **114**(3): p. 717-30.
69. Nierman, W.C., et al., *Complete genome sequence of *Caulobacter crescentus**. 2001. **98**(7): p. 4136-4141.
70. Marks, M.E., et al., *The Genetic Basis of Laboratory Adaptation in *Caulobacter crescentus**. 2010. **192**(14): p. 3678-3688.
71. Rossmann, F.M., et al., *In situ structure of the Caulobacter crescentus flagellar motor and visualization of binding of a CheY-homolog*. 2020. **114**(3): p. 443-453.
72. Nesper, J., et al., *Cyclic di-GMP differentially tunes a bacterial flagellar motor through a novel class of CheY-like regulators*. *eLife*, 2017. **6**: p. e28842.
73. House, B., et al., *Acid-stress-induced changes in enterohaemorrhagic Escherichia coli O157:H7 virulence*. 2009. **155**(9): p. 2907-2918.

74. Minamino, T., et al., *Effect of Intracellular pH on Rotational Speed of Bacterial Flagellar Motors*. 2003. **185**(4): p. 1190-1194.
75. Smith, J.J., J.P. Howington, and G.A. McFeters, *Survival, physiological response and recovery of enteric bacteria exposed to a polar marine environment*. *Appl Environ Microbiol*, 1994. **60**(8): p. 2977-2984.
76. Beales, N., *Adaptation of Microorganisms to Cold Temperatures, Weak Acid Preservatives, Low pH, and Osmotic Stress: A Review*. *Comprehensive Reviews in Food Science and Food Safety*, 2004. **3**(1): p. 1-20.
77. Vorob'eva, L.I., *Stressors, Stress Reactions, and Survival of Bacteria: A Review*. *J Applied Biochemistry and Microbiology*, 2004. **40**(3): p. 217-224.
78. Benjamin, M.M. and A.R. Datta, *Acid tolerance of enterohemorrhagic Escherichia coli*. *Appl Environ Microbiol*, 1995. **61**(4): p. 1669-1672.
79. Fallingborg, J., *Intraluminal pH of the human gastrointestinal tract*. *J Danish medical bulletin*, 1999. **46**(3): p. 183-196.
80. Zilberstein, D., et al., *Escherichia coli intracellular pH, membrane potential, and cell growth*. *Journal of bacteriology*, 1984. **158**(1): p. 246-252.
81. Jin, Q. and M.F. Kirk, *pH as a Primary Control in Environmental Microbiology: I. Thermodynamic Perspective*. *Front Environ Sci*, 2018. **6**(21).
82. Padan, E., D. Zilberstein, and S. Schuldiner, *pH homeostasis in bacteria*. *Biochimica et Biophysica Acta (BBA) - Reviews on Biomembranes*, 1981. **650**(2): p. 151-166.

83. Hall, H.K., K.L. Karem, and J.W. Foster, *Molecular responses of microbes to environmental pH stress*. *Adv Microb Physiol*, 1995. **37**: p. 229-72.
84. Booth, I.R., *Regulation of cytoplasmic pH in bacteria*. *Microbiological reviews*, 1985. **49**(4): p. 359-378.
85. Booth, I.R. and R.G. Kroll, *Regulation of cytoplasmic pH (pH_i) in bacteria and its relationship to metabolism*. *Biochem Soc Trans*, 1983. **11**(1): p. 70-2.
86. Slonczewski, J.L., et al., *Cytoplasmic pH Measurement and Homeostasis in Bacteria and Archaea*, in *Advances in Microbial Physiology*, R.K. Poole, Editor. 2009, Academic Press. p. 1-317.
87. Foster, J.W. and M.P. Spector, *How Salmonella survive against the odds*. *Annu Rev Microbiol*, 1995. **49**: p. 145-74.
88. Fang, F.C., et al., *The alternative sigma factor katF (rpoS) regulates Salmonella virulence*. *Proc Natl Acad Sci*, 1992. **89**(24): p. 11978-11982.
89. Chen, J., et al., *Lmo0036, an ornithine and putrescine carbamoyltransferase in Listeria monocytogenes, participates in arginine deiminase and agmatine deiminase pathways and mediates acid tolerance*. *Microbiology*, 2011. **157**(11): p. 3150-3161.
90. Lin, J., et al., *Comparative analysis of extreme acid survival in Salmonella typhimurium, Shigella flexneri, and Escherichia coli*. *J Bacteriol*, 1995. **177**(14): p. 4097-104.

91. Booth, I. and R.G. Kroll, *The preservation of foods by low pH*. Mechanisms of Action of Food Preservation Procedures. Elsevier Applied Science, 1989: p. 119-160.
92. Lund, P., A. Tramonti, and D. De Biase, *Coping with low pH: molecular strategies in neutralophilic bacteria*. FEMS Microbiology Reviews, 2014. **38**(6): p. 1091-1125.
93. Hughes, B.S., A.J. Cullum, and A.F. Bennett, *Evolutionary Adaptation To Environmental Ph In Experimental Lineages Of Escherichia Coli*. Evolution, 2007. **61**(7): p. 1725-1734.
94. Bulthuis, B.A., et al., *The relation of proton motive force, adenylate energy charge and phosphorylation potential to the specific growth rate and efficiency of energy transduction in Bacillus licheniformis under aerobic growth conditions*. Antonie van Leeuwenhoek, 1993. **63**(1): p. 1-16.
95. Slonczewski, J.L., et al., *Effects of pH and Repellent Tactic Stimuli on Protein Methylation Levels in Escherichia coli*. J Bacteriol, 1982. **152**(1): p. 384-399.
96. Stijlemans, B., et al., *Development of a pHrodo-based assay for the assessment of in vitro and in vivo erythrophagocytosis during experimental trypanosomosis*. PLoS neglected tropical diseases, 2015. **9**(3): p. e0003561-e0003561.
97. Sträuber, H. and S. Müller, *Viability states of bacteria—Specific mechanisms of selected probes*. Cytometry A, 2010. **77A**(7): p. 623-634.
98. Campbell, T.N. and F. Choy, *The effect of pH on green fluorescent protein: A brief review*. Molecular Biology Today, 2001. **2**: p. 1-4.

99. Ward, W.W., et al., *Spectral Perturbations of the Aequorea Green-Fluorescent Protein*. *Photochemistry and Photobiology*, 1982. **35**(6): p. 803-808.
100. Chattoraj, M., et al., *Ultra-fast excited state dynamics in green fluorescent protein: multiple states and proton transfer*. *Proc Natl Acad Sci* 1996. **93**(16): p. 8362-8367.
101. Brejc, K., et al., *Structural basis for dual excitation and photoisomerization of the Aequorea victoria green fluorescent protein*. *Proc Natl Acad Sci U S A*, 1997. **94**(6): p. 2306-11.
102. Young, B., et al., *pH-sensitivity of YFP provides an intracellular indicator of programmed cell death*. *Plant Methods*, 2010. **6**(1): p. 27.
103. Llopis, J., et al., *Measurement of cytosolic, mitochondrial, and Golgi pH in single living cells with green fluorescent proteins*. *Proceedings of the National Academy of Sciences of the United States of America*, 1998. **95**(12): p. 6803-6808.
104. Shen, Y., et al., *pHuji, a pH-sensitive red fluorescent protein for imaging of exo- and endocytosis*. *Journal of Cell Biology*, 2014. **207**(3): p. 419-432.
105. Wilks, J.C. and J.L. Slonczewski, *pH of the Cytoplasm and Periplasm of Escherichia coli: Rapid Measurement by Green Fluorescent Protein Fluorimetry*. *J Bacteriol*, 2007. **189**(15): p. 5601-5607.
106. Olsen, K.N., et al., *Noninvasive Measurement of Bacterial Intracellular pH on a Single-Cell Level with Green Fluorescent Protein and Fluorescence Ratio Imaging Microscopy*. *Appl Environ Microbiol*, 2002. **68**(8): p. 4145-4147.

107. Morimoto, Y.V., et al., *High-Resolution pH Imaging of Living Bacterial Cells To Detect Local pH Differences*. *mBio*, 2016. **7**(6).
108. Martinez, K.A., et al., *Cytoplasmic pH Response to Acid Stress in Individual Cells of Escherichia coli and Bacillus subtilis Observed by Fluorescence Ratio Imaging Microscopy*. *Appl Environ Microbiol*, 2012. **78**(10): p. 3706-3714.
109. Awaji, T., et al., *Novel Green Fluorescent Protein-Based Ratiometric Indicators for Monitoring pH in Defined Intracellular Microdomains*. *Biochemical and Biophysical Research Communications*, 2001. **289**(2): p. 457-462.
110. Rosado, C., et al., *Rosella: A fluorescent pH-biosensor for reporting vacuolar turnover of cytosol and organelles in yeast*. *Autophagy*, 2008. **4**(2): p. 205-213.
111. Hanson, G.T., et al., *Green fluorescent protein variants as ratiometric dual emission pH sensors. 1. Structural characterization and preliminary application*. 2002. **41**(52): p. 15477-15488.
112. Martynov, V.I., et al., *Genetically encoded fluorescent indicators for live cell pH imaging*. *Biochimica et Biophysica Acta (BBA) - General Subjects*, 2018. **1862**(12): p. 2924-2939.
113. dos Anjos, C., et al., *Antimicrobial blue light inactivation of international clones of multidrug-resistant Escherichia coli ST10, ST131 and ST648*. *Photodiagnosis and Photodynamic Therapy*, 2019. **27**: p. 51-53.
114. Lipovsky, A., et al., *Visible light-induced killing of bacteria as a function of wavelength: Implication for wound healing*. *Lasers in Surgery and Medicine*, 2010. **42**(6): p. 467-472.

115. Maclean, M., et al., *Inactivation of Bacterial Pathogens following Exposure to Light from a 405-Nanometer Light-Emitting Diode Array*. Applied and Environmental Microbiology, 2009. **75**(7): p. 1932-1937.
116. Dai, T., et al., *Blue light for infectious diseases: Propionibacterium acnes, Helicobacter pylori, and beyond?* Drug resistance updates : reviews and commentaries in antimicrobial and anticancer chemotherapy, 2012. **15**(4): p. 223-236.
117. Wang, Y., et al., *Antimicrobial blue light inactivation of pathogenic microbes: State of the art*. Drug resistance updates : reviews and commentaries in antimicrobial and anticancer chemotherapy, 2017. **33-35**: p. 1-22.
118. Abana, C.M., et al., *Characterization of blue light irradiation effects on pathogenic and nonpathogenic Escherichia coli*. MicrobiologyOpen, 2017. **6**(4): p. e00466.
119. Parkinson, J.S., *Complementation analysis and deletion mapping of Escherichia coli mutants defective in chemotaxis*. Journal of Bacteriology, 1978. **135**(1): p. 45-53.
120. ADLER, J. and B. TEMPLETON, *The Effect of Environmental Conditions on the Motility of Escherichia coli*. Microbiology, 1967. **46**(2): p. 175-184.
121. Yuan, J., et al., *Adaptation at the output of the chemotaxis signalling pathway*. Nature, 2012. **484**(7393): p. 233-236.

122. Yang, J., et al., *Biphasic chemotaxis of *Escherichia coli* to the microbiota metabolite indole*. Proceedings of the National Academy of Sciences, 2020. **117**(11): p. 6114-6120.
123. Baird, G.S., D.A. Zacharias, and R.Y. Tsien, *Biochemistry, mutagenesis, and oligomerization of DsRed, a red fluorescent protein from coral*. Proceedings of the National Academy of Sciences of the United States of America, 2000. **97**(22): p. 11984-11989.
124. Bencina, M., *Illumination of the spatial order of intracellular pH by genetically encoded pH-sensitive sensors*. Sensors (Basel), 2013. **13**(12): p. 16736-58.
125. VanEngelenburg, S.B. and A.E. Palmer, *Fluorescent biosensors of protein function*. Current Opinion in Chemical Biology, 2008. **12**(1): p. 60-65.
126. Lele, P.P., et al., *Mechanism for adaptive remodeling of the bacterial flagellar switch*. Proc Natl Acad Sci, 2012. **109**(49): p. 20018-20022.
127. Chawla, R., K.M. Ford, and P.P. Lele, *Torque, but not FliL, regulates mechanosensitive flagellar motor-function*. Scientific Reports, 2017. **7**(1): p. 5565.
128. Lele, P.P. and H.C. Berg, *Switching of bacterial flagellar motors triggered by mutant FliG*. Biophysical journal, 2015. **108**(5): p. 1275-1280.
129. Bednarska, N.G., et al., *Protein aggregation in bacteria: the thin boundary between functionality and toxicity*. 2013. **159**(Pt_9): p. 1795-1806.
130. Li, H. and V. Sourjik, *Assembly and stability of flagellar motor in Escherichia coli*. Molecular Microbiology, 2011. **80**(4): p. 886-899.
131. Purcell, E.M. *Life at Low Reynolds Number*. 1977.

132. Blair, K.M., et al., *A molecular clutch disables flagella in the Bacillus subtilis biofilm*. Science, 2008. **320**(5883): p. 1636-8.
133. Darnton, N.C., et al., *On Torque and Tumbling in Swimming *Escherichia coli**. Journal of Bacteriology, 2007. **189**(5): p. 1756-1764.
134. Shrivastava, A., P.P. Lele, and H.C. Berg, *A rotary motor drives Flavobacterium gliding*. Current biology : CB, 2015. **25**(3): p. 338-341.
135. Turner, L., et al., *Visualizing Flagella while Tracking Bacteria*. Biophysical Journal, 2016. **111**(3): p. 630-639.
136. Schneider, W.R. and R.J.J.o.b. Doetsch, *Effect of viscosity on bacterial motility*. 1974. **117**(2): p. 696-701.
137. Ford, K.M., et al., *Switching and Torque Generation in Swarming E. coli*. 2018. **9**(2197).
138. Lighthill, J., *Flagellar hydrodynamics*. SIAM review, 1976. **18**(2): p. 161-230.
139. Johnson, R.E., *An improved slender-body theory for Stokes flow*. Journal of Fluid Mechanics, 1980. **99**(2): p. 411-431.
140. Chattopadhyay, S. and X.-L. Wu, *The effect of long-range hydrodynamic interaction on the swimming of a single bacterium*. Biophysical journal, 2009. **96**(5): p. 2023-2028.
141. Rodenborn, B., et al., *Propulsion of microorganisms by a helical flagellum*. Proceedings of the National Academy of Sciences, 2013. **110**(5): p. E338-E347.
142. Najafi, J., et al., *Swimming of bacterium Bacillus subtilis with multiple bundles of flagella*. Soft Matter, 2019. **15**(48): p. 10029-10034.

143. Valeriani, C., et al., *Colloids in a bacterial bath: simulations and experiments*. Soft Matter, 2011. **7**(11): p. 5228-5238.
144. Diethmaier, C., et al., *Viscous drag on the flagellum activates Bacillus subtilis entry into the K-state*. Molecular microbiology, 2017. **106**(3): p. 367-380.
145. Li, G. and J.X. Tang, *Low Flagellar Motor Torque and High Swimming Efficiency of *Caulobacter crescentus* Swarmer Cells*. Biophysical Journal, 2006. **91**(7): p. 2726-2734.
146. Shapiro, L.J.A.r.o.c.b., *Generation of polarity during Caulobacter cell differentiation*. 1985. **1**(1): p. 173-207.
147. Berne, C., Y.V. Brun, and G. O'Toole, *The Two Chemotaxis Clusters in Caulobacter crescentus Play Different Roles in Chemotaxis and Biofilm Regulation*. 2019. **201**(18): p. e00071-19.
148. Briegel, A., et al., *Activated chemoreceptor arrays remain intact and hexagonally packed*. 2011. **82**(3): p. 748-757.
149. Xie, L., et al., *Bacterial flagellum as a propeller and as a rudder for efficient chemotaxis*. 2011. **108**(6): p. 2246-2251.
150. Antani, J.D., et al., *Asymmetric random walks reveal that the chemotaxis network modulates flagellar rotational bias in Helicobacter pylori*. eLife, 2021. **10**: p. e63936.
151. Lele, P.P., et al., *Response thresholds in bacterial chemotaxis*. 2015. **1**(9): p. e1500299.

152. Hansen, M.C., et al., *Assessment of GFP fluorescence in cells of Streptococcus gordonii under conditions of low pH and low oxygen concentration*. 2001. **147**(5): p. 1383-1391.
153. Degnen, S.T. and A. Newton, *Chromosome replication during development in Caulobacter crescentus*. Journal of Molecular Biology, 1972. **64**(3): p. 671-680.
154. Thanbichler, M., A.A. Iniesta, and L. Shapiro, *A comprehensive set of plasmids for vanillate- and xylose-inducible gene expression in Caulobacter crescentus*. Nucleic Acids Research, 2007. **35**(20): p. e137-e137.
155. Hottes, A.K., et al., *Transcriptional profiling of Caulobacter crescentus during growth on complex and minimal media*. Journal of bacteriology, 2004. **186**(5): p. 1448-1461.
156. Lele, P.P., et al., *The flagellar motor of Caulobacter crescentus generates more torque when a cell swims backward*. Nat Phys, 2016. **12**(2): p. 175-178.
157. Lauga, E., et al., *Swimming in circles: motion of bacteria near solid boundaries*. Biophys J, 2006. **90**(2): p. 400-12.
158. Yang, J., et al., *Biphasic chemotaxis of Escherichia coli to the microbiota metabolite indole*. 2020. **117**(11): p. 6114-6120.
159. Mesibov, R. and J. Adler, *Chemotaxis toward amino acids in Escherichia coli*. J Bacteriol, 1972. **112**(1): p. 315-26.
160. Jani, S., et al., *Chemotaxis to self-generated AI-2 promotes biofilm formation in Escherichia coli*. 2017. **163**(12): p. 1778-1790.

161. Jani, S., *Visualizing chemoattraction of planktonic cells to a biofilm*, in *Bacterial Chemosensing*. 2018, Springer. p. 61-69.